Torque spectroscopy for the study of rotary motion in biological systems

Lipfert, J; van Oene, MM; Lee, M; Pedaci, Francesco; Dekker, NH

DOI
10.1021/cr500119k

Publication date
2015

Document Version
Accepted author manuscript

Published in
Chemical Reviews

Torque Spectroscopy for the Study of Rotary Motion in Biological Systems

Jan Lipfert[1,2], Maarten M. van Oene[2], Mina Lee[2], Francesco Pedaci[2,3], and Nynke H. Dekker[2]

[1]Department of Physics, Nanosystems Initiative Munich, and Center for NanoScience (CeNS), Ludwig-Maximilian-University Munich, Amalienstrasse 54, 80799 Munich, Germany

[2]Department of Bionanoscience, Kavli Institute of Nanoscience, Delft University of Technology, Lorentzweg 1, 2628 CJ Delft, The Netherlands

[3]Department of Single-Molecule Biophysics, Centre de Biochimie Structurale, UMR 5048 CNRS, Montpellier, France

TABLE OF CONTENTS

1. INTRODUCTION

To understand the mechanistic basis of cellular function, immense efforts are undertaken to investigate the many different molecules that constitute a cell, aiming to both probe individual molecules as well as their interactions with others. Our understanding of the molecular basis of e.g. genome processing (including transcription, translation, and replication), the cytoskeleton and its dynamics, membrane assembly and composition, and cellular motion has grown tremendously in recent decades. Underlying the dynamics of many of these interactions are highly specialized enzymatic processes that facilitate specific chemical reactions. When these reactions are coupled to mechanical motion, the enzymes that perform the mechano-chemical couplings are referred to as molecular machines, since they transduce chemical energy into mechanical work. DNA and RNA polymerases and helicases, protein translocases, kinesins and myosins etc. are well-known examples of such molecular machines. Many such machines employ forces to execute linear motion, but it is also possible for a molecular machine to generate torques and to execute rotary motion. Indeed, in processes as distinct as bacterial swimming and the copying of DNA during replication, rotational motion and accompanying torques play key roles.

It is now possible to study in detail, at the level of individual molecules, the workings of the underlying molecular machines, yielding insight into the different ways that torque is generated and rotary motion is executed in biological systems. This area of research, which we denote torque spectroscopy by analogy with the force spectroscopy that is

used to investigate linear motion and accompanying forces at the single-molecule level in biological systems, is rapidly expanding its range due to a wealth of technical advances that have been made in recent years. In this Review, we describe the methods that have been developed to monitor the generation of torque and the rotary motion of individual molecular machines and highlight a number of recent examples of how such single-molecule methods have shaped our understanding of rotary motion in biologically relevant molecular machines.

An illustrative example to appreciate the importance of rotary processes at the molecular level is the double-helical nature of DNA (**Figure 1a**), famously discovered by Watson and Crick.[1] Already at the time of the discovery of its structure, scientists appreciated that the helical nature of the DNA would have important implications for its processing and read-out during transcription or replication. Indeed, unwinding of the DNA double helix in order to access the genetic information results in rotational motion and the generation of the torsional strains.[2] Such torsional strains, in turn, cause supercoiling of the DNA,[3] which is defined as a change of the DNA linking number away from its intrinsic, torsionally relaxed helicity of one turn per 10.5 base pairs. Supercoiling can lead to the formation of plectonemes (**Figure 1b**) or completely alter the structure of DNA away from its canonical B-form (see **Section 5**). In particular, negative supercoiling tends to open the double helix and to separate the DNA strands, facilitating e.g. transcription initiation.[4] While torsional strains are generated in DNA through the active, dynamic motion of translocases, such as polymerases[2b,5] and helicases (**Figure**

1c), DNA supercoiling also serves a passive, quasi-static role in DNA compaction. In eukaryotes, DNA is wrapped around histone proteins forming nucleosomes[6] and higher order chromatin structures.[7] In prokaryotes, DNA is less compacted than in eukaryotes, but there are still a number of proteins that wrap DNA, such as HNS and HU.[8] Cells have evolved dedicated enzymes that can control and alter the topological state of supercoiled DNA, including topoisomerases that can relax supercoiling[9] and gyrases that can generate positive supercoiling. *In vivo*, DNA supercoiling is tightly regulated,[10] with the supercoiling density (defined as the excess linking number of DNA divided by its intrinsic helicity) approximately maintained at -0.05. DNA supercoiling serves important regulatory functions at the level of transcription and growth.[11]

In addition to DNA-processing enzymes that control maintenance and replication of the genome, one also finds examples of rotary machines that operate within the context of cellular membranes. A key molecular machine that executes rotary motion is the F_0F_1-ATPase that is responsible for the synthesis of ATP inside of the mitochondrial matrix, providing the source of energy for most cellular metabolism[12] (**Figure 1d**,**e**). The F_0F_1-ATPase is composed of two coupled motors, F_0 and F_1, each of which can independently execute rotary motion.[13] The F_0 motor is integrated into the membrane and its rotary motion is driven by proton gradients. Remarkably, this rotary motion is then employed to drive F_1, resulting in the synthesis of ATP[14] (**Figure 1d**). Conversely, reverse motion of the F_1 motor, fueled by ATP hydrolysis, can serve to restore the proton-motive force (**Figure 1e**). Other rotary motors that are phylogenetically related to F_0F_1-ATPase include

the flagellar type III ATPase FliI (similar to the F_1-ATPase subunits[14]), the rotary motors involved in the flagellar export apparatus,[15] and (a Mg^{2+}) transporter(s).[16]

Box 1. Magnitudes of forces and torques in biological systems. Forces are expressed in Newtons (N), with the magnitudes of the forces that play a role in biological systems on the sub-cellular scale typically falling in the range of pN to nN. This can be qualitatively understood from the argument that the relevant energy scale is that of the thermal fluctuations (k_BT; ≈ 4 pN·nm at room temperature) and that the relevant length scales are in the range of nm, the ratio of these two quantities yielding the force scales. A typical molecular machine such as *E. coli* RNA polymerase is capable of applying forces of ~25 pN on average.[17] Torques are expressed in Newton·meters (N·m), with the magnitudes of the torques that play a role in biological systems on the sub-cellular scale falling in the range of tens to thousands of pN·nm. This can be understood from the magnitude of the typical forces mentioned above multiplied by the lengths of lever arms which are again in the range of nm. For example, the same RNA polymerase is capable of applying torques up to 11 pN·nm.[5,18]

Numerous approaches have contributed to our understanding of rotational processes in molecular biology, including analytical techniques such as two-dimensional gel electrophoresis (in particular to probe the supercoiled state of DNA molecules[19]), spectroscopic approaches such as circular dichroism and single-molecule polarization spectroscopy[20] (e.g. to probe molecular handedness), and structural techniques such as

electron microscopy[21] and x-ray crystallography.[22] This review, however, focuses particularly on the recent development and use of single-molecule approaches that rely on the manipulation and readout of microscopically sized transducers attached to biological systems. These approaches, which include the use of e.g. atomic force microscopy, *optical tweezers*, and *magnetic tweezers* (**Section 2** and **Box 4**), are capable of operating in the native aqueous environment of biological systems and are able to read out changes in the physical properties of biological molecules as they occur, i.e. in real time. They have primarily been used to monitor or impose changes in linear extension of molecules, and to control and read out the corresponding parameter of force. As attested by multiple review articles in the Special Issue to which this Article is linked, these developments, which can collectively be grouped under the header of force spectroscopy, have led to many new insights into the mechanics of biological molecules and the nanometer-sized molecular machines that operate on them. These force spectroscopy techniques are increasingly complemented with techniques that can read out or manipulate the angular coordinates and the accompanying torques directly, ushering in an era of single-molecule torque spectroscopy.

In this review, we focus on the development of single-molecule techniques to probe and manipulate the rotational degrees of freedom in biological systems. In **Section 2**, we give an overview of the different types of techniques that can be used to apply and measure torque and twist in biological systems. In **Section 3**, we describe in more detail the magnetic tweezers-based approaches that have been utilized most frequently in

biological investigations. In **Section 4**, we highlight polarization-based optical approaches that have been used to investigate the role of torque on single molecules. In **Section 5**, we discuss recent applications of the now very powerful techniques of torque spectroscopy, and we conclude with an outlook towards future developments in **Section 6**.

2. SINGLE-MOLECULE APPROACHES FOR THE MEASUREMENT OF TWIST AND TORQUE

Numerous methods have been developed for the measurement of twist and torque in biological systems, which we review here. A schematic overview of the twist and torque measuring methods is shown in **Figure 2**.

2.1. Tracking of rotational motion. The conceptually simplest approach to monitoring twist and torsional properties in biological systems has been to simply track rotational motion, without manipulating it actively. In order to be able to monitor rotational motion at the molecular scale and to achieve the angular resolution relevant for biological questions, it is often necessary to tether the molecule or biological complex of interest between a surface and a (sub)micron-sized object that can be tracked to provide the angular readout. The fluctuating environment of aqueous solution at ambient temperatures provides a (at least in principle) calibrated probe of torsional properties via rotational Brownian motion, even in the absence of any ability to apply externally controlled forces or torques.

An early example of the rotary tracking approach is the work of Berg, Berry, and coworkers who have extensively studied many aspects of the bacterial flagellar motor, bacterial locomotion, and chemotaxis, by either attaching the flagellum to a surface and tracking the rotating cell body[23] (**Figure 2a**) or by attaching the cells to a surface and tracking fluorescently labeled flagella[24] or beads attached to the flagellum.[25] In the latter approach, it is possible to systematically vary the load by using beads of different sizes[25a,26] or by employing media of different viscosities:[25b,26b] both approaches alter the torsional drag.

Kinosita and coworkers pioneered early applications of rotational tracking to single molecules *in vitro.* They were able to determine the torsional stiffness of actin filaments from the rotational fluctuations of bead duplexes attached to suspended filaments.[27] In general, the rotational stiffness k_θ can be determined from the width of the angular fluctuations using the equipartition theorem:

$$k_\theta = k_B T / Var(\theta) \quad \textbf{(Equation 1)}$$

where k_B is Boltzmann's constant, T the absolute temperature and $Var(\theta)$ the variance of the angle fluctuations $Var(\theta) = < (\theta(t) - < \theta >)^2 >$, where $< \cdots >$ denotes the time average. The measured rotational trap stiffness k_θ is related to the intrinsic torsional stiffness C of the system by:[27-28]

$$k_\theta = k_B T \; C/L_C = C'/L_C \; \textbf{(Equation 2)}$$

where L_C is the contour length of the molecule (or the effective contour length for the suspended attachment geometry of Kinosita and coworkers[27]). C is the measured (or "effective") torsional persistence length in units of length; alternatively some authors prefer C', the torsional stiffness in units of energy times length.

In another pioneering study, Kinosita and coworkers attached an actin filament to the γ-subunit of F_1-ATPase to directly visualize its rotation[29] (**Figure 2b**). By analyzing motors with attached actin filaments of different lengths, providing different amounts of viscous drag, a simple estimate of the motor's load dependence and torque generation could be obtained. Improvements of the assay using a fast camera to image small (40 nm) gold beads attached to the F_1-ATPase γ-subunit enabled the resolution of rotational sub-steps and the investigation of the hydrolysis rate dependence on load.[30] A more recent study exploiting rotational tracking employed bead dumbbells (i.e. pairs of beads) tethered to a surface by double-stranded DNA to monitor EtBr intercalation and the concomitant unwinding of DNA[31] (**Figure 2c**).

Motors from the kinesin and dynein families can induce rotational motion and apply torques in addition to linear motion along their microtubule tracks. The rotational motion of kinesin and dynein on microtubules has been studied by direct tracking using increasingly sophisticated assays. Pioneering studies used the intrinsic curvature in filaments to visualize rotation induced by 14S dynein[32] and *Drosophila claret* segregation protein[33] in sliding filament assays. More recent work employed

polystyrene beads labeled with smaller fluorescent marker beads (somewhat similar to the bead geometry shown in **Figure 2g**) to probe the rotational motion of kinesin bound to microtubules[34] or an optical trapping apparatus to suspend microtubules and to visualize the rotational motion induced by a number of kinesin variants linked to "cargo" beads.[35]

2.2. Electrorotation. Whereas much can be learned by simply observing the rotational motion of biological systems of interest, be it passive Brownian motion or rotation actively driven by molecular motors, the ability to apply external forces and torques provides additional dimensions of inquiry. One simple approach to applying torque is electrorotation (**Figure 2d**), which can be applied to any dielectric object.[36] The principle of electrorotation relies on the fact that an electric field can induce a polarization in a dielectric object. Such an induced polarization will be co-linear with the applied electric fields at low frequencies but, due to the presence of frequency-dependent losses (resulting from the time required to redistribute charges), this will no longer be the case at high frequencies (in the MHz range). Consequently, there will be a phase lag between the field and induced dipole moment that results in the presence of a time-averaged torque. This torque, whose magnitude can be controlled by the strength of the electric field, the rotation frequency, the particle radius, as well as the electrical properties of both the particle and the fluid, can be made sufficiently large to spin micron-sized cells at speeds of several hundred Hz[37] and has been used to study the response to applied torque of both the flagellar motor of tethered *E. coli* cells[38] and the F_1-ATPase motor.[39]

In the context of flagellar motor manipulation, the technique of electrotation appeared particularly advantageous, since it did not require the addition of handles or labels to the bacterial cell. However, its application to this cellular system in particular has been hampered by variations in the applied torque as a function of cell angle, which renders the data analysis somewhat cumbersome.[40]

2.3. Magnetic tweezers. *Magnetic tweezers* (**Box 4**) (MT) are a versatile single-molecule technique that permits the application of both forces and torques to biological macromolecules and their complexes (**Figure 2f-j**). The various implementation of MT are all based on attaching micron-sized superparamagnetic beads or particles to the biological assembly of interest. The superparamagnetic particles, in turn, can be manipulated by magnetic fields that are generated by permanent and/or electromagnets. MT have many strengths, including overall simplicity and robustness of the experimental implementation, facile application of torque, natural operation and straightforward calibration in constant force mode,[41] extension to parallel measurements,[42] and absence of sample heating and photodamage.[43] Compared to other single-molecule approaches,[44] MT provide a way to perform force-dependence measurements at forces as low as ≈ 10 fN.

Conventional magnetic tweezers (**Figure 2f**) most frequently use pairs of permanent magnets to apply both forces and torques to magnetic beads tethered to a flow cell surface by a molecule of interest, often double-stranded DNA or other nucleic acid

constructs[9d,41,45] (alternate experimental configurations that rely on the use of electromagnets are described in Refs.[46]). In this configuration, the magnetic field tightly constraints the rotation of the bead about the tether axis; the externally controlled rotation of the magnets effectively sets the linking number or "number of applied turns" of the tethered molecule. In this conventional configuration, MT do not track rotational motion directly, and, while they apply torque, they do not measure torque directly. Instead, twist and in some cases torque can be measured or inferred indirectly.

For example, in the plectonemic regime for double-stranded DNA[45a,47] or RNA,[48] there is an approximately linear relationship between the measured tether length and the linking number (**Figure 7c**). In this regime, a change in linking number by one turn results in a change in the tether length by approximately 50 nm (with the exact value depending on applied stretching force, salt concentration of the buffer, and other experimental variables). Therefore, relatively small changes in linking number can be reliably detected by monitoring the magnetic bead position above the surface. This tether length-to-linking number correspondence has been used extensively to study DNA-processing enzymes at the single-molecule level. Examples include studies of the activity of topoisomerase type II,[49] topoisomerase IA,[50] topoisomerase IB,[51] topoisomerase V,[52] RNA polymerase,[53] ligase,[54] and a serine recombinase.[55]

Similar to using the tether length-to-linking number conversion to infer changes in molecular twist, analysis of the rotation vs. extension behaviour can be used to

indirectly determine torque.[51a,52,55-56] While these indirect methods are powerful due to their simplicity (requiring only position tracking of the bead and straight-forward post-processing of the data), they are limited, as they -explicitly or implicitly- require assumptions about a particular model of supercoiling in nucleic acids. For example, it is typically assumed that the molecular torque is constant in the plectonemic regime,[51a,52,54,56-57,57b] an assumption that has been challenged particularly in the regimes of low salt or low forces by recent theoretical work.[58] Perhaps more importantly, the indirect approaches to deducing torque and twist fail in situations where the process under study directly alters the structure and properties of nucleic acid tether, e.g. in the case of filament assembly on or small-molecule binding to DNA.[59]

2.4. Tracking rotational motion while applying forces. To overcome the limitations of conventional MT, several variants of MT have been developed that expand or modify the capabilities of the conventional assay.[46b,56b,59c,60] One general approach has been to employ permanent magnets with a (at least approximately) vertically aligned field such that the bead's rotation about the vertical tether axis is unconstrained or only weakly constrained by the magnets. Using image processing to track rotation, sometimes in combination with modified beads to introduce an asymmetry, these assays are similar to methods based on rotational tracking alone, with the difference that controlled stretching forces can be applied. The ability to apply controlled stretching forces is useful, since the applied force is often a control parameter of interest; in addition, even

moderate stretching forces are efficient in keeping the bead away from the flow cell surface, to avoid surface interactions and non-specific sticking.

The *freely-orbiting magnetic tweezers* **(Box 4)** (FOMT; **Figure 2i**) are one implementation of this general approach. Importantly, in the FOMT the fluctuation pattern of the bead is used to align the magnets such that the barrier to full rotation of the bead becomes much less than the thermal energy $k_B T$. To date, the FOMT assay has found application in the study of RecA[28b] and Rad51 assembly[59d] and has been used to measure the torsional stiffness of DNA by determining equilibrium angular fluctuations[28b] (**Section 5**). Even with less well aligned magnets changes in the twist of nucleic acids tethers can be detected, if the processes driving the rotation are sufficient to overcome small residual energy barriers to full rotation. Examples for applications of such FOMT-like (i.e. without precise alignment of the magnets) MT assays include studies of the rotation induced by RNA-polymerase,[18] the branch-migration of a Holiday junction,[61] and Rad51 assembly on DNA.[62]

A conceptually related experimental scheme that affords enhanced spatio-temporal resolution is the *rotor-bead assay* (**Box 4**)(**Figure 2e**). Here, a non-magnetic bead is attached to a specifically labeled position along a DNA tether. The motion of this rotor-bead around the DNA tether axis can be tracked via video microscopy (in some cases using fluorescence) to provide an angular read out. In addition, its rotational motion can be calibrated against the known viscous drag of a bead rotating around an axis through

its equator. Additional beads attached to the ends of the DNA tether are used to apply controlled stretching forces. An early implementation of the rotor-bead assay used optical tweezers together with a micropipette to stretch the DNA and was used to measure the torsional properties of DNA[28a] (**Figure 2e** and **Section 3**). The rotor-bead technique was subsequently simplified by integrating it with magnetic tweezers (**Figure 2j**) to apply forces and rotations and has been successfully used to study the DNA twist-stretch coupling,[63] DNA structural transitions,[64] and gyrase activity.[65] Most recently, the assay has been further improved by replacing the rotor-bead with a gold-nanoparticle and employing fast tracking using backscattering and evanescent nanometry.[66] Conceptually, the FOMT can be thought of as a variant of the rotor-bead assay, in which the magnetic bead functions both as the rotor bead and to apply stretching forces to the tether. The FOMT assay is simpler than the rotor-bead assay in the sense that no internal modifications to the tethered DNA are required and that only a single bead is employed. However, since the magnetic bead that provides the angular readout also needs to be of sufficient size to apply forces (typically of the order of several pN), its size is typically larger than state-of-the-art rotor beads, which reduces the achievable temporal resolution (for additional details, see **Section 3**).

2.5. Magnetic torque tweezers. Finally, in recent years several variants of magnet tweezers have been developed that, similar to conventional MT, constrain the free-rotation of the magnetic beads but, unlike conventional MT, can directly measure torque. Such *magnetic torque tweezers* (**Box 4**) (MTT; **Figure 2g**) share several common

developments that facilitate the measurement of torque, namely the introduction of an angular asymmetry in the magnetic bead or particle for the measurement of the rotation angle about the tether axis and, compared to conventional MT, a weaker angular trap that confines the orientation of the magnetic particle.[46b,59c,60a,67] This weaker angular trap, intermediate in its torsional stiffness between the FOMT and the MT, makes it possible to measure shifts in the mean angular position that result from the accumulation of torque in a twisted, tethered molecule. Such weak angular traps rely on the addition of a small horizontal field component to a predominantly vertically aligned field (**Figure 2g**). Further details of the implementations and capabilities of MTT are discussed in **Section 3.**

A drawback of currently available torque measurement schemes is the intrinsic coupling between the force and torque degrees of freedom: for example, current MTT instruments employ permanent magnets that control both the stretching force and the rotational trapping potential.[59c,60a] This has resulted in the development of the electromagnetic torque tweezers[68] (eMTT, **Figure 2h**). The eMTT combine permanent and electromagnets to enable the application of a wide range of stretching forces (from < 10 fN to tens of pN), while independently controlling the torsional trap stiffness of the instrument (from zero up to several pN·μm/rad). This is advantageous for torque measurements, as it allows matching of the torsional trap stiffness of the instrument to the characteristic torques of the molecule or molecular complex under study.[59c,67-68] In addition, being able to rapidly change trap stiffness affords experimental flexibility, e.g.

to alternate between rapid changes of molecular twist (using a high trap stiffness, as in the MT) and sensitive torque measurements (using a lower trap stiffness, as in the MTT). Finally, the eMTT provide a bridge between instruments designed to measure torque, such as the variants of the MTT discussed above, and instruments designed to measure twist, as they can also operate as FOMT, by reducing the current in the additional coils to zero.

2.6. Optical torque tweezers. Complementing the magnetic tweezers assays, developed to apply and measure torque on biological systems, are optical approaches (**Figure 2k-n**). These optical approaches rely on the fact that light carries momentum in addition to energy, and that light-matter interactions can result in energy and momentum transfer. When the linear momentum of light is modified by the interaction with a scattering object, a force on the object is exerted, an effect that is harnessed in optical tweezers, in which the forces due to the intensity gradient near a tight laser focus dominate the scattering force in the direction of beam propagation. Optical tweezers allow for the trapping of microscopic particles in three dimensions[69] and have been extensively used for their manipulation. Interested readers are referred to several excellent reviews.[70]

The functionality of optical tweezers can be expanded to include the exertion of torque, as demonstrated by the development of several types of *optical torque tweezers* (**Box 4**). The conceptually simplest implementation relies on the application of forces in an asymmetrical manner about a point of rotation (**Figure 2k**). For example, a common

approach is to rotate the trapping beam with respect to the point of rotation while using an object as a lever arm of length r, with a resulting torque Γ equal to $r \times F$. Several variations of this approach have been used to study biophysical properties while applying an external torque to the bacterial flagellar motor[71] (**Figure 2k**). Alternative lever arm-based approaches include the use of pairs of polystyrene beads,[72] the use of two beams to rotate a pair of fused silica beads about an axis perpendicular to the axis connecting the beads (allowing the rotation axis to be oriented at will[73]), or the use of a paddle-wheel, in which two laser traps maintain the rotation axis of the paddle-wheel while a third beam pushes the paddle.[74]

An alternative way in which optical traps can apply torque exploits the fact that light can carry *orbital angular momentum.*[75] Typically, the lasers employed in optical traps operate in the fundamental TEM_{00} transverse mode, characterized by a Gaussian intensity distribution (in which the *Poynting vector* (**Box 4**) and the wave vector are both perpendicular to the wavefront and parallel to the collimated beam axis). Alternatively, it is possible to generate beams with controlled helical wave fronts[76] (where the Poynting vector and the wave vector spiral about the beam axis[75b]). As a consequence, the Poynting vector and wave vector have an azimuthal component in addition to their component in the direction of beam propagation, which implies a non-zero angular momentum about the beam axis. As such a helical phase front is accompanied by an annular intensity distribution with zero intensity on-axis, particles that are larger than the beam annulus will be trapped at the beam center and undergo on-axis rotation,[75c]

whereas particles that are smaller than the beam annulus will be trapped by the higher intensity annulus and orbit about the beam axis[75c,77] (**Figure 2l**). The transfer of orbital angular momentum relies on modulation of the beam's phase structure,[78] which can occur either through the absorption or scattering of photons. The first realization of such a beam with well-defined orbital angular momentum was achieved by Allen and colleagues.[79] In 1995 Rubinsztein-Dunlop and coworkers demonstrated the transfer of angular momentum onto micron-sized particles.[80]

A third way for light beams to apply torque utilizes their ability to carry spin angular momentum (**Figure 2m**,**n**). Whereas the orbital angular momentum is determined by a beam's spatial distribution, the spin angular momentum of light depends on the fraction of photons occupying the $\sigma = +1$ and $\sigma = -1$ spin states. For example, left- (right-) circularly polarized light is composed of photons occupying exclusively the state $\sigma = +1\ (-1)$, with linearly polarized light resulting from an equal measure of left- and right-circularly polarized components. The transfer of spin angular momentum relies on light-matter interactions that alter the polarization state of the light, either through selective absorption of photons or their scattering (including reflection and refraction). A convenient way to demonstrate the existence of the spin angular momentum of light (predicted by Poynting in 1909) is through the use of birefringent materials (e.g. anisotropic crystals) that have the property to modify the polarization of light (with little or no absorption) as their *index of refraction* (**Box 4**) depends on light's polarization and direction of propagation. This was exploited by Beth[81] in 1936, who measured the

transfer of spin angular momentum from a circularly polarized beam onto a one-inch circular quartz wave plate.[81] Many years later, Rubinsztein-Dunlop and colleagues repeated this experiment at the microscopic scale, by optically trapping micron-sized calcite particles[82] that acted similarly to the wave plate employed by Beth. These particles could then be rotated using either linear or circular polarization (**Section 4**). The same approach, enhanced by an advanced polarization control system and a detection system for quantitative torque measurements, was implemented by La Porta and Wang[83] (**Figure 2n**). An alternative approach that relies on the squeezing of polystyrene spheres into disks to introduce *birefringence* (**Box 4**) into micron-sized particles was utilized by Ormos and colleagues[84] (**Figure 2m**).

3. MEASURING SINGLE-MOLECULE TORQUE AND TWIST USING MAGNETIC TWEEZERS

We now discuss some of the principles underlying magnetic tweezers based torque and twist measurements and highlight practical aspects that can guide users in the selection of the appropriate techniques for a particular biological question of interest. Applications of these techniques to DNA are subsequently discussed in **Section 5**.

3.1. Application of forces and torques in magnetic tweezers. All magnetic tweezers implementations rely on the fact that both forces and torques can be applied to magnetic beads or particles attached to macromolecular assemblies of interest by applying external magnetic fields. Importantly, the applied forces and torques depend on different properties of the field and of the particles and can, therefore, be (largely)

decoupled. The force F exerted on a paramagnetic particle by an external field B is given (at least approximately) by:

$$F = \frac{1}{2} grad(m(B) \cdot B) \qquad \textbf{(Equation 3)}$$

where $m(B)$ is the induced magnetization and *grad* is the gradient operator.[41,85] Thus, the force depends essentially on the gradient of magnetic field. In conventional magnetic tweezers (**Figure 2f**), the field direction lies in the (x, y) -plane, while the field gradient and, therefore, the force are in the z-direction. In typical MTT or FOMT implementations, in contrast, the field and its gradient typically point along the z-direction, such that again an upward stretching force is applied in the direction of the z-axis. The magnitude of the force depends on the magnitude of the field gradient and the induced magnetization $m(B)$, which is a material property of the magnetic particles. Most magnetic tweezers measurements employ commercially available superparamagnetic beads, which consist of small ferromagnetic nanoparticles embedded in a non-magnetic polymer matrix. Typical combinations of commercially available beads and permanent magnets achieve forces in the range of 0.01 – 100 pN, with higher forces being possible if large (> 3 µm diameter) beads are employed. Forces are typically determined from thermal fluctuations, using the relationship:

$$F = k_B T \, L/Var(x) \qquad \textbf{(Equation 4)}$$

where $k_B T$ is the thermal energy, L is the tether length (typically evaluated as the mean distance from the surface $L = < z >$) and $Var(x)$ is the variance of the in-plane fluctuations. In practice, it is best to evaluate $Var(x)$ not by simply computing the variance of the x-time trace, but by analyzing the x-fluctuations in Fourier space, since

this allows to reduce the influence of drift and to correct for a number of artifacts introduced by the finite acquisition frequency of the camera.[86] In the MTT and FOMT, **Equation 4** needs to be slightly modified by replacing the x-fluctuations in the denominator with in-plane fluctuations in the radial coordinate, see below. In addition to calibrating the forces from thermal fluctuations, they can be computed from first principles based on calculations of the magnetic fields[41] and taking into account the induced magnetization $m(B)$ by evaluating **Equation 3**. Since most magnetic tweezers experiments employ permanent magnets as mentioned earlier, the forces are varied by controlling the distance of the magnets to the sample.

The torque exerted by the magnetic field Γ_{B} in magnetic tweezers is given by:

$$\Gamma_{\mathrm{B}} = m_0 \times B \qquad \textbf{(Equation 5)}$$

where the direction of m_0 defines the anisotropy axis of the particle. In typical magnetic tweezers experiments, the rotation of the bead and the application of torque are controlled by rotating the magnetic field, usually by simply rotating the permanent magnets. The torque depends on the field direction (see Section 3.4.) and on the anisotropy of the magnetic particle. We note that for the purpose of the force calculations for commercially available superparamagnetic beads, one can neglect the anisotropy and consider the beads as paramagnetic. A perfect, "text-book" paramagnetic bead, however, could not be rotated by a (slowly) rotating magnetic field, since it does not have a preferred magnetization axis; rotating the field would only rotate the induced magnetization, but not lead to physical rotation of the bead. The

ability to apply torque and to rotate beads in the magnetic tweezers, therefore, relies on the magnetic particles having a preferred magnetization axis. The exact nature of this anisotropy is still debated. While some authors have been able to account for their data (obtained at relatively low fields) by using a model with a small permanent (i.e. ferromagnetic) magnetization component in addition to the induced paramagnetic component,[68] other have argued that beads have a "soft" magnetization axis, i.e. that there is no magnetization in the absence of any external fields but that the beads have a preferred magnetization axis.[87] Such a soft axis model for magnetization is somewhat analogous to the (electric) polarizability of a birefringent material. Seidel and coworkers were able to account for their indirect measurements of the torsional trap stiffness over a larger field range in conventional magnetic tweezers using a soft axis model.[88] Nonetheless, mixed models combining aspects of a soft axis and permanent magnetization components have also been proposed.[89] Nonetheless, it is clear that the superparamagnetic beads used in magnetic tweezers experiments have a preferred axis and that it is this anisotropy that permits the application of torques.

3.2. Principle of torque measurements in magnetic torque tweezers. Fundamentally, magnetic torques tweezers measure torque by tracking the rotation angle of the bead or attached particle and by analyzing shifts in the mean angular position in a calibrated angular trap (**Figure 3a**). In the MTT, the rotation of the bead about the tether axis is constrained by a weak angular trap. The equilibrium position of the angular track, θ_0, is given by the mean of the angle, averaged over thermal fluctuations (**Figure 3b**). The

stiffness of the angular trap k_θ, in turn, can be calibrated from the thermal fluctuations about that equilibrium position (**Equation 1**). After applying a number N turns by rotating the bead through a rotating magnetic field, the tether exerts a restoring torque Γ_{tether} that can be determined by simply multiplying the shift in the mean angle position by the angular trap stiffness:

$$\Gamma_{\text{tether}} = -k_\theta < \theta_N - \theta_0 > \qquad \textbf{(Equation 6)}$$

The torque measurement is akin to reading off a force from a spring scale calibrated against thermal fluctuations, an approach used -for example- to calibrate AFM cantilevers or optical traps, except that it considers linear extension instead of shifts in angle and force instead of torque. In practice, the challenge is to choose k_θ such that the shifts $< \theta_N - \theta_0 >$ corresponding to the torques typically exerted by biological macromolecules are detectable with the experimentally achieved spatiotemporal angle resolution.

3.3. Angular tracking. For the measurement of twist and torque in magnetic systems (**Figure 2g-i**), it is necessary to track the angular orientation of the magnetic bead or particle that is attached to the macromolecular tether of interest. Typically, angular tracking is achieved by analysis of CCD camera images, either using simple bright-field images or possible additional fluorescent markers. A complication for angle tracking is the fact that commercially available superparamagnetic beads are nearly spherically symmetric. While it is possible to track small intrinsic asymmetries in the bead images,[88,90] more robust angle tracking is afforded by either using custom made

assemblies of magnetic particles,[60a] dumbbells of two beads,[46b] or by attaching small non-magnet beads to the magnet beads to act as fiducial markers. The latter approach enables simultaneous tracking of the (x, y, z) and angle positions with an angular resolution of $\sigma_{\theta,tracking} \sim 0.1°$ as judged by tracking magnetic beads carrying smaller fiducial marker beads that are stuck to a surface[60b] (**Figure 4a,b**). This level of angular resolution is close to the optimum expected for micron-size particles based on considerations of optical position resolution.[46b,60b] The tracking error intrinsically limits the torque resolution to $\sigma_\Gamma \approx k_\theta \, \sigma_{\theta,tracking}$. This fundamental limitation makes it necessary to alter the magnet geometry compared to conventional magnetic tweezers to reduce the rotational trap stiffness, in order to enable measurements of biologically relevant torques (**Box 1** and see below).

In addition to tracking the particles rotation directly by analysis of the CCD images, there is a second elegant method that can be used to measure the rotation angle of tethered spherical magnetic beads. While being conceptually slightly more involved than the direct image-based angle tracking, it has the advantage of being robust and not requiring any additional preparatory steps compared to conventional magnetic tweezers (such as the attachment of non-magnetic fiducial beads). This approach exploits the tethering geometry in magnetic tweezers with a mostly vertically aligned field, i.e. in the MTT and FOMT approaches (**Figure 2g**, left inset and **Figure 2h,i**). The preferred axis of the bead aligns along the (mostly) vertical field direction; at the same time, the bead is pulled upwards, towards the magnets. In this geometry, the (x, y)-fluctuations of the

bead lie on a circular annulus, whose radius is given by the tether attachment point in relationship to the beads preferred magnetization axis (**Figure 2g**, left inset). The center of the bead fluctuates about the attachment point, such that the same face of the bead always points towards the center of the fluctuation "doughnut". If the bead is tethered by the "south pole" in relationship to the preferred magnetization axis, the annulus traced out by the (x, y)-fluctuations has zero radius and the alternative tracking approach fails; if the bead is, however, tethered somewhere away from the south pole, its (x, y)-fluctuations trace out a circular annulus with a radius approximately equal (or somewhat smaller) than the bead radius R_{bead}. After fitting a circle with radius R and center position (x_0, y_0) to the (x, y)-fluctuations, the instantaneous (x_i, y_i)-position can be converted to polar coordinates (r_i, θ_i):

$$r_i = \sqrt{(x_i - x_0)^2 + (y_i - y_0)^2} \qquad \textbf{(Equation 7)}$$

$$\theta_i = arctan\left(\frac{y_i - y_0}{x_i - x_0}\right)$$

The advantage of this method is that in terms of tracking software and bead preparation, it does not require any steps beyond the requirements of conventional magnet tweezers measurements. A disadvantage is that the linear Brownian motion gives rise to apparent angle fluctuations that depend on tether length, stretching force, and bead radius. The achievable angle resolution is, therefore, reduced compared to direct angle tracking approaches. In the FOMT geometry, this loss in angle resolution is typically negligible, as the angular fluctuations are large. In contrast, in the MTT, the

angular fluctuations are typically more narrow and, therefore, cross-talk of the (x, y)-fluctuations with the angle coordinate can result in an underestimation of the rotational trap stiffness and needs to be taken into account. Nonetheless, the resolution of the (x, y) -based angle tracking is sufficient for torque measurements with an appropriately chosen torsional trap stiffness.[68]

3.4. Angular trap stiffness. In conventional tweezers, the field direction is in the (x, y)-plane (**Figure 2f**) and, therefore, the rotational motion about the tether axis (along the z-axis) is tightly constrained. As a result, angular fluctuations are in the range of ~1° (**Figure 4a,c**), corresponding to rotational trap stiffnesses for rotation about the tether axis in the range of 10^4-10^5 pN · nm/rad (unless only very small stretching forces are required). Given that the torque resolution is fundamentally limited by $\sigma_\Gamma \approx k_\theta \, \sigma_{\theta,tracking}$ and that $\sigma_{\theta,tracking} \geq 10^{-2} - 10^{-3}$ rad (see above), the torque resolution in conventional magnetic tweezers is very limited and mostly unsuited for biological torque measurements that require a resolution of ~10 pN · nm or better. To enable biologically relevant torque measurements it is, therefore, necessary to change the magnet geometry compared the conventional magnetic tweezers configuration to achieve a lower rotational trap stiffness.

One approach to reducing the angular trap stiffness about the tether axis is to use a magnet geometry where the magnetic field is mostly aligned with the *z*-axis, as in most standard MTT configurations and in the eMTT[59c,60a,67-68] (**Figure 2g**). This altered magnet

geometry reduces the trap stiffness for rotation about the *z*-axis by approximately two orders-of-magnitude compared to conventional magnetic tweezers to 100-1000 pN · nm/rad, corresponding to fluctuations of ~10° (**Figure 4a,d**), as the preferred magnetization axis of the particle is now mostly aligned along the *z*-axis. The reduced trap stiffness for rotation about the tether axis, in turn, enables torque measurements with ~1 pN · nm torque resolution. An alternative approach to reducing the rotational trap stiffness is to employ electromagnets with time varying magnetic fields,[46b] however, this approach is currently limited by the small achievable stretching forces.

If vertically oriented magnets are carefully aligned above the tether attachment point, the bead's rotation about the tether axis is no longer constrained by the magnets in this so-called FOMT configuration (**Figure 2i**) and the rotational trap stiffness due to the magnets becomes negligible. The FOMT alignment requires positioning of the magnets with ~µm accuracy and can be achieved by using the rotational fluctuations as a sensitive read out of the local potential.[28b] Any residual rotational trapping due to the magnets gives rise to preferred angular positions with a one turn periodicity. Under a well-aligned vertical magnet in the FOMT, the bead's rotation is constrained only by the torsional stiffness of the tether and the rotational trap stiffness is given by **Equation 1**. For ~kbp length DNA constructs, the corresponding trap stiffness is in the range of 0.1 pN · nm/rad, another two order-of-magnitude reduction compared to the MTT configuration, corresponding to fluctuations with a width of 100s of degrees (**Figure 4a,e**). The FOMT geometry is ideally suited to follow processes that alter the twist of

nucleic acid tethers, such as advancing polymerases[18] or the assembly of nucleo-protein complexes.[59c,d,62] Its angular resolution is limited by the intrinsic width of the fluctuations and, importantly, by the time scale of the measurements, as discussed in the next sub-section.

3.5. The characteristic timescales of rotational motion. To complete our description of magnetic systems used for the measurement of twist and torque, we discuss the characteristic timescales of the systems involved, since these determine the degree to which an experimentalist can observe short-lived changes in torque or twist and set the measurement time required to detect a given angle or torque signal. The characteristic timescale for rotational motion in an angular trap can be analytically derived by realizing that the behavior of the rotational degree of freedom $\theta(t)$ of a microscopic tethered bead in aqueous solution can be described by an overdamped Langevin equation:

$$\gamma_\theta \frac{d\theta(t)}{dt} + k_\theta(\theta(t) - \theta_0) = \Gamma_{\mathrm{therm}}(t) \qquad \textbf{(Equation 8)}$$

Here, γ_θ is the rotational friction coefficient, k_θ is the rotational trap stiffness, and $\Gamma_{\mathrm{therm}}(t)$ is a Langevin torque from random collisions of the particle with the solvent. Since the collisions are uncorrelated on the time scale of our measurement $\Gamma_{\mathrm{therm}}(t) \sim \delta(t)$. $\theta_0 = <\theta(t)>$ is the equilibrium angle of the trap, with the angled brackets denoting the time average. Choosing our coordinate system such that $\theta_0 = 0$, we define the autocorrelation function $R(\tau)$ as:

$$R(\tau) = <\theta(t)\theta(t+\tau)> = \lim_{t_{total}\to\infty} \frac{1}{t_{total}} \int_0^{t_{total}} \theta(t)\theta(t+\tau)\, dt. \qquad \textbf{(Equation 9)}$$

It can be shown that $R(\tau)$ satisfies:

$$\gamma_\theta \frac{dR(\tau)}{d\tau} + k_\theta R(\tau) = 0 \qquad \textbf{(Equation 10)}$$

with the solution:

$$R(\tau) = \frac{k_B T}{k_\theta}\ exp\left[-\frac{k_\theta}{\gamma_\theta}\tau\right] = \frac{k_B T}{k_\theta}\ exp\left[-\frac{\tau}{\tau_C}\right] \quad \textbf{(Equation 11)}$$

where $\tau_C = \gamma_\theta / k_\theta$ defines the characteristic time scale of the system and the pre-factor stems from the fact that the autocorrelation for zero time is equal to the variance of the angle, which by the equipartition theorem is equal to the absolute temperature divided by the trap stiffness. Determination of τ_C by fitting an exponential decay to the temporal autocorrelation data (**Figure 4f**) for the different magnetic tweezers configurations shows that the characteristic time scales for rotational motion vary by several orders of magnitude, as expected from the variation in angular trap stiffness k_θ. Using similar ~µm sized beads, conventional magnetic tweezers have a typical rotational temporal response of $\tau_C <$ 0.1 s, the MTT have a temporal response of τ_C ~0.1-1 s, and the FOMT have a response time of τ_C ~ 10-1000 s, due to the large differences in rotational trap stiffnesses.

An alternative approach to determining the characteristic time scale of the rotational motion is to analyze the power spectrum of the angular fluctuations. The power spectral density (PSD) of the angular fluctuations can be fit to a Lorentzian:[70e,83]

$$\mathrm{PSD}(f) = \frac{A}{1 + (f/f_C)^2} \quad \textbf{(Equation 12)}$$

where *A* is the amplitude and f_C is the characteristic frequency of the system equal to $k_\theta / 2\pi\gamma_\theta$, which can be related to its characteristic time scale using $2\pi f_C = \omega_C$ and $\omega_C = 1/\tau_C$ (**Figure 4g**).

The rotational friction coefficient for a sphere of radius R_{bead} rotating about an axis offset by R_{circle} from its center in a medium of viscosity η is given by (neglecting corrections for a finite distance to a flow cell surface,[28b,91] appropriate when the distance between the sphere and the surface exceeds R_{bead}):

$$\gamma_\theta = 8\pi\eta {R_{bead}}^3 + 6\pi\eta {R_{circle}}^2 R_{bead} \qquad \textbf{(Equation 13)}$$

Importantly, the friction coefficient grows approximately with the cube of the bead size (**Table 1**). In particular for FOMT measurements, it is therefore very advantageous to use the smallest possible beads (**Table 1**). The strong particle size dependence of the friction coefficient and thus characteristic time scale of rotational motion also makes the use of a separate rotor bead or nano-particle advantageous,[28a,63,65a] since separation of force application and rotational tracking makes possible the use of small beads (< 100 nm radius) or even gold nanoparticles for angular tracking.[64,66]

4. OPTICAL TORQUE TWEEZERS FOR SINGLE MOLECULE TORQUE MEASUREMENTS

In this section, we highlight aspects of the optical trapping systems that users will find most useful in guiding their implementations for particular experiments. We first focus on the general properties of suitable particles, and subsequently discuss torque application and detection, with a particular focus on the case of spin angular momentum.

4.1. The types of particles used in optical tweezers. The most straightforward way to transfer momentum from light to matter is by means of absorption, and to this end black ceramic powder,[80] CuO particles,[92] weakly absorbing Teflon particles,[93] and others have been employed. However, while this approach benefits from its conceptual simplicity, a significant disadvantage is the intrinsic coupling between absorption and a high scattering force. This makes trapping in the direction of beam propagation challenging without additional means to oppose the scattering force. Another disadvantage of the use of absorption is the accompanying heating of the particles, which may not only change the properties of the particle itself but also those of the surrounding medium.[94]

Thus, the more frequent approach is to use transparent particles. In conventional optical tweezers, spherically-shaped polystyrene beads and silica beads are usually objects of choice because of their low absorption and high refractive index, which allow trapping in aqueous media. Transparent beads can also be used for optical angular manipulation, in the context of transfer of orbital angular momentum, when a beam carrying orbital angular momentum propels them about the beam axis.[95] More frequently, however, transparent particles adopting more complex shapes or formed from different materials are employed in optical tweezers to exploit their asymmetry in the interaction with the trapping beam. For example, asymmetrically scattering particles have been engineered and rotated in an optical trap.[96] Such micro-propellers can be readily fabricated using the two-photon polymerization of resins and include 100-nm sized features.[78,97] For rotation using transfer of orbital angular momentum, the

transparent particle needs to be designed to alter the transverse phase distribution of the focused beam, effectively acting as a microscopic mode converter[73]. For the transfer of spin angular momentum to transparent particles, the defining property is birefringence, and birefringent particles can be thought of as microscopic wave plates in this context.[98] The sources of birefringence are quite diverse and include *crystal anisotropy* (**Box 4**),[82-83] *shape anisotropy* (**Box 4**),[84,99] magneto-optic effects,[87,100] electro-optic effects,[100] and mechanical stresses.[100]

4.2. Considerations in selecting a type of optical torque spectroscopy. When selecting between the different torque spectroscopy approaches, one considers the complexity of the different particle types, the ease of setting up the technique, and the necessity to accurately detect torque, amongst others. For example, the conceptually straightforward lever-arm approaches of torque application in which one uses an optical trap to move one end of a lever arm with respect to a point of rotation (**Section 2** and **Figure 2k**) benefits from the use of the commercially available transparent polystyrene or silica particles discussed above. The required movement about the point of rotation can be accomplished in a number of ways (e.g. laser beams can be moved using e.g. an acousto-optic deflector,[72,101] galvanometric[102] or piezoelectric mirrors, or spatial light modulators;[103] conversely, the sample stage itself can be moved, leaving the beam path unaltered[71a]), and the position of the particle inside the calibrated trap can then be read out to yield first the force, and hence the applied torque according to $\Gamma = r \times F$ (where r is the distance to the point of rotation). However, this approach relies on the

attachment of the lever-arm if it is not naturally available. Alternatively, one can select the approach that relies on the transfer of orbital angular momentum, which comes at the expense of requiring either more complex particles to induce the transfer of orbital angular momentum from Gaussian beams (ways of shaping the trapped particle have already been discussed above), or the shaping of the input beam so that it carries orbital angular momentum on incidence (**Section 2** and **Figure 2l**). The latter requirement can be accomplished using spiral phase plates, holograms,[76] or the placement of cylindrical lenses.[75d] However, this approach suffers from challenges in the detection of the transferred torque: while it is readily defined as being equal to the output angular momentum minus the input angular momentum, the determination of in particular the angular momentum content of the output beam is frequently limiting. For biophysical experiments in which it is desirable both to apply torque as well as to measure it precisely, the approaches based on the transfer of spin angular momentum have proven to be most fruitful (**Section 2** and **Figure 2m,n**), despite their reliance on complex properties of materials such as birefringence. We therefore focus on these approaches, starting with their underlying physical concepts.

4.3. The concepts of polarization and birefringence. To appreciate the role of birefringence, it is useful to understand the polarization properties of light. Collimated laser beams operated in the fundamental TEM_{00} transverse mode have electric and magnetic field components that oscillate (at a frequency ω) orthogonally to each other and to the direction of propagation.[104] If its electric field oscillates in a plane, light is said

to be linearly polarized. This linear polarization can be decomposed into two orthogonal linear components that oscillate in phase (**Figure 5a**). If these orthogonal linear components are equal in amplitude but are shifted by a relative phase difference of $\pi/2$, the resulting electric field vector rotates and the light is said to be circularly polarized (with left- and right-circularly polarized light differing in the direction of the rotation). Most generally, light can be elliptically polarized, with the electric field vector tracing out an ellipse. Alternatively, a polarization state can be decomposed into two orthogonal circular components, which can be associated with the spin of photons; $\sigma = +1$ or -1, having an angular momentum of $+\hbar$ or $-\hbar$, respectively. Thus any polarization state can be associated with a spin angular momentum, $\sigma\hbar$, where σ can range between -1 and 1. In this representation linear polarization is associated with an equal amplitude for the two orthogonal circular components, with a net σ equal to zero.

A material is said to be *birefringent* when its refractive index (**Box 4**) depends on the polarization and propagation direction of the light. The different indices of refraction can be visualized by an index ellipsoid (**Figure 5b**). In this representation, an isotropic material with identical indices of refraction along all axes (e.g. the commonly used polystyrene beads) is shown as a sphere. If only two of the three indices are equal, the material is said to have a single optic axis, i.e. to be uniaxial. In a uniaxial birefringent material, the extraordinary axis with index of refraction n_e is parallel to the optic axis, while the two ordinary axes with index of refraction n_o are perpendicular to the optic axis. The birefringence of such a material is defined as $\Delta n = n_e - n_o$. This value can be

positive (e.g. quartz) or negative (e.g. calcite) and the uniaxial material is likewise classified as positive or negative birefringent. When all three indices differ, the material has two optic axes and is said to be biaxial.

The birefringence of particles results in the ability to apply torque using polarized light. This can be easily seen for particles with $r \gg \lambda$ (the regime of ray optics) as well as for particles with $r \ll \lambda$ (the regime of wave optics). In the ray optics regime, assuming that the optic axis is perpendicular to the direction of propagation, one can decompose the light's polarization along the particle's extraordinary and ordinary axes. Since these polarization components travel at different velocities through the material, one of the components acquires a phase delay of $kd\Delta n$ with respect to the other[105] (here k is the wavenumber and d the thickness of the material, see **Box 2** and **Figure 5c**). As a result of the passage through the particle, the light's polarization state changes, an effect exactly analogous to the one of a wave plate, resulting in a redistribution of photons with $\sigma = \pm 1$, i.e. in the transfer of spin angular momentum. In the wave optics regime, we can approximate the material as a point polarizability,[106] in which case the light's electric field will induce an electric dipole moment p equal to αE, where α is the electric polarizability tensor (a function of the extraordinary and ordinary electric susceptibilities χ_e and χ_o or, equivalently, the refractive indices n_e and n_o). As a result of birefringence, p and E are not collinear, therefore an optical torque $\Gamma = p \times E$ acts on the material (**Figure 5d**). Torque will also be applied in the intermediate regime ($r \approx \lambda$), but the argumentation in this limit relies on additional calculations.[107]

4.4. Sources of birefringence. We limit our discussion of the sources of birefringence to the two best-known ones, namely crystal anisotropy[82-83] and shape anisotropy,[84,99] as these have formed the basis of particles utilized in optical torque spectroscopy. Crystal anisotropy originates in an anisotropy in the binding forces within a crystal lattice. As light propagates by exciting atoms in the medium by its electric field, a difference in binding forces will result in differences in propagation velocities, which can bring about a change of the polarization state of the light. Three well-known birefringent crystals that have found diverse applications include calcite, vaterite, and quartz. Calcite is a form of calcium carbonate that has a negative uniaxial birefringence[108] ($\Delta n = -0.163$ at $\lambda_0 = 1064$ nm). Vaterite is a different form of calcium carbonate that has a positive uniaxial birefringence[109] ($\Delta n = 0.100$). An apparent disadvantage of vaterite for biological experiments is its increased solubility in water compared to calcite. However, when functionalized, vaterite particles can be stabilized in water up to several hours[109b] (**Figure 5e**). Quartz is a silicon dioxide compound with a smaller positive uniaxial birefringence[108] ($\Delta n = 0.009$ at $\lambda_0 = 1064$ nm). Its advantages include inertness in physiological conditions and suitability for nanofabrication. Multiple recipes have been published for the fabrication of quartz cylinders suitable for optical torque tweezers experiments (**Figure 5f**). These approaches use either optical, electron-beam or nanosphere lithography to pattern an array of round dots to selectively protect materials from reactive ion etching, resulting in the creation of cylinders.[99b,110] Typically, such cylinders can then be selectively functionalized on one face for biomolecule

attachment. Cylinders can also be fabricated to include a small, centered protrusion that can form the sole functionalized component, a procedure that improves the on-axis attachment of biomolecules to the cylinder and its on-axis rotation.[99b,110b]

Birefringence resulting from shape anisotropy occurs in particles that are composed of inherently isotropic materials but have adopted particular shapes and dimensions. For example, when a particle has dimensions that are on the order of or less than λ, it will be more easily polarizable along its most extended axis. For example, a wavelength-sized disk-shaped particle will readily align its flat faces with the laser polarization (**Figure 2m**), which provides a straightforward means to dictate its angular orientation using linearly polarized laser light. Such disks can simply be produced by mechanically squeezing isotropic polystyrene spheres[84,99b] (**Figure 5h**). Provided that the polystyrene spheres are initially coated, biomolecules can then be tethered to the disks, providing further confinement (**Figure 2m**). However, it is important to realize that tethering to the face of the disks, which is statistically favored given uniform coating, can provoke off-axis tethering: hence, careful selection may be required. The same principle can be used to trap and rotate sub-100 nm gold nanorods[94a] (**Figure 5i**), whose extended axes will align with the incident laser polarization (**Figure 5j**).

4.5. Maximizing a birefringent particle's angular confinement in all three dimensions. When relying on the transfer of spin angular momentum to apply and read out torque, it is beneficial to fix two of the particle's rotational degrees of freedom while controlling

the third. The scattering force can be used to confine either one (disks, **Figure 2m**) or two (cylinders, **Figure 2n**) rotational degrees of freedom, since the extended axis or axes will align with the beam axis provided that the particle size is sufficiently large compared to the beam size[111] (**Figure 5g**). The third rotational degree of freedom (about the beam axis) can then be controlled using the polarization. For a particle with negative birefringence, linearly polarized incident light will cause the extraordinary axis to be repelled from the electric field vector E, thereby confining a single rotational degree of freedom. For a particle with positive birefringence, the extraordinary axis is attracted to the electric field vector E, thereby confining two rotational degrees of freedom (a situation that is analogous to the rotational confinement of magnetic beads by an external magnetic field, **Section 3**). Hence, in the case of a quartz cylinder with positive birefringence fabricated in such a way that its extraordinary axis lies in a plane orthogonal to the cylinder's axis (**Figure 5f**), the scattering force and polarization both contribute to the alignment of the cylinder with the beam axis, while rotation about the beam axis is controlled by the polarization input alone.

4.6. Practical considerations in the application and detection of optical torque using spin angular momentum. Linearly polarized optical torque tweezers will force a birefringent particle to align with the linear polarization, providing an angular clamp that is highly analogous to the position clamp provided by linear optical tweezers. Rotation of this linear polarization can be used to either orient the particle or to apply an optical torque. The general expression for the torque on the birefringent particle (**Box 2**)

reduces to the simple formula $\Gamma = \Gamma_0 \sin(2\theta)$ for the case of linear polarization ($\phi = 0$). Here Γ_0, the maximum torque, is a function of the laser power, the degree of birefringence and the particle size (**Figures 6a,b**, blue lines). When the polarization is rotated, the particle will tend to align with the polarization, but as it experiences an opposing drag torque, there will be an angular separation between the applied polarization and the particle axis (**Figure 6c.i**). If the polarization rotation rate is increased, the drag torque on the particle increases and hence the angle between particle and polarization increases. At a critical polarization rotation speed, the optical torque can no longer overcome the drag torque. Interestingly, the particle does not escape the angular trap (in contrast to the case of translational trapping), since the trap is periodic. Rather, a phase slip between the particle's extraordinary axis and the polarization results, appearing as a spike in the torque signal (**Figure 6c.ii**). At even higher polarization rotation rates, the particle fails entirely to respond to the rotating laser polarization, resulting in a periodic torque signal (**Figure 6c.iii**). The same response, but now averaged over multiple cycles, is shown in **Figure 6d**. Interestingly, such behavior of a birefringent cylinder inside a rotating angular trap can be analytically described as an excitable system.[112]

Box 2. Magnitude of torque transfer using spin angular momentum. As light passes through a birefringent material, its polarization state may change to a degree that depends on the initial polarization of the input beam (whether it is circular, elliptical or linear), the angle between a linear component of the polarization and extraordinary

axis, and the thickness of the material. The optical torque per unit area that can be applied by a beam that passes through a material of uniform thickness (for $\lambda < r$, where r is the dimension of the scattering particle) is given by:[82,105,107a]

$$\Gamma = -A \sin \Delta_p \cos 2\phi \sin 2\theta + A \left(1 - \cos \Delta_p\right) \sin 2\phi \qquad \textbf{(Equation 14)}$$

Here, $A = \frac{\epsilon c}{2\omega} E_0^2$, where ϵ is the permittivity, c is the speed of light, ω is the angular frequency of light, and E_0 is the electric field amplitude. The acquired phase delay Δ_p is equal to $kd(n_o - n_e)$, where k is the wavenumber, d the thickness of the material, and n_o (n_e) the ordinary (extraordinary) index of refraction, as above. The incoming polarization is described by ϕ; notably, for $\phi = 0$ or $\pi/2$ the light is linearly polarized, whilst for $\phi = \pi/4$ or $3\pi/4$ the light is circularly polarized. Thus, the first term describes the contribution of the linear part of the polarization (the part in which circular components are balanced), and for a purely linearly polarized input beam, the torque is proportional to $\sin(2\theta)$, where θ is the angle between the extraordinary axis of the birefringent material and the linear polarization. Conversely, the second term describes the contribution of the circular part of the polarization (the excess of either one of the circular components).

The optical torque as a function of θ for different polarization states ϕ is plotted in **Figure 6a**. This shows that while the torque resulting from the linear part of the polarization reduces to zero when a birefringent particle adopt a specific angular orientation (stable points indicated by the filled black circles on the blue curves), the torque resulting from the circular part of the polarization will remain fixed independent

of the particle's angular orientation (red curves). Shown in **Figure 6b** is the torque as a function of d for both linear (blue curve; here $\theta = \pi/4$ for maximal torque) and circular (red) polarizations. One observes that the achievable torque is higher when linear polarization is used together with thin birefringent particles; however, provided thicker birefringent particles are available, the use of circular polarization ultimately achieves the highest applicable torques.

There are several ways to provide the polarization rotation required to exert torque in a linearly polarized optical torque tweezers. The most straightforward approach relies on the use of a motorized $\lambda/2$ waveplate: rotation of the waveplate by a specific angle results in a rotation of the polarization by twice this angle. However, disadvantages of this approach are limitations on the maximum speed of rotation as well as accompanying vibration. A more sophisticated approach splits a single beam into two beams with orthogonal polarizations using a polarizing beam splitter, and passes each through an acousto-optic modulator to generate a relative phase shift between them. Recombining the two beams and passing them through a $\lambda/4$ waveplate regenerates a linear polarization whose orientation can be controlled by the relative phase shift induced by the acousto-optic modulators.[83] This approach can be simplified by replacing the two acousto-optic modulators by a single electro-optic modulator that induces a phase shift between two perpendicular polarization components[99b,112] (**Figure 6f.i**). In this manner, rapid and stable control of the incoming laser polarization can be obtained.

The detection of the amount of spin angular momentum transferred can readily proceed via measurements of laser polarization. The angular momentum transferred from the light to the particle is equal and opposite to momentum transferred from the particle to the light. Thus, measurement of both the angular momentum in the input beam and the angular momentum after transmission through the particle provides a good measure for the optical torque transferred,[105a] $\Gamma = \left(\sigma_{z,in} - \sigma_{z,out}\right)P/\omega$, P is the laser power and ω is the angular frequency of the laser light. When the polarization input is linear, $\sigma_{z,in} = 0$. The polarization output can be measured as an imbalance between the left and right circular components,[105a] i.e. $\sigma_{z,out} = (P_L - P_R)/P$, such that the transferred torque is given by[83] $\Gamma = (P_R - P_L)/\omega$. The left and right circular polarization components can be measured by putting a $\lambda/4$ wave plate at the output of the trap, converting the circular components into linear components, which can be split by a polarizing beam splitter and their respective powers can be measured by photodiodes (**Figure 6f.ii**).

In practice the torque is not calculated from $\Gamma = (P_R - P_L)/\omega$, but the signal from the photodetectors $(P_R - P_L)$ is used to calibrate the system. The calibration provides 1) a conversion factor, converting the voltage output of the photodetector to picoNewton nanometer; 2) a drag coefficient, especially if the particle is non-spherical; and 3) the angular stiffness or equivalently the maximum torque. Five different methods of calibration have been proposed.[113] The methods vary in the number of polarization rotation frequencies that should be measured, but they all have in common that they

perform three independent measurements: a measurement of the angular thermal fluctuations; a measurement of the angular response to a controlled modulation of the angular trap; and a measurement of the characteristic time scale of the system. These three independent measurements are sufficient to provide the three parameters to be calibrated. As an example, taking the standard deviation of multiple torque traces taken at different polarization rotation rates (like the traces in **Figure 6c.i-iii**) results in **Figure 6e**. Here the low rotation speeds provide a measurement of the thermal noise, the high speeds give the response to a known angular modulation, and the transition point between these regimes is a measure for the characteristic time.

The linearly polarized optical torque tweezers can function not only as an angular clamp, but also as a torque clamp. In one such approach, the polarization detectors measure the torque transferred to the particle and send this signal to a control loop. This loop adjusts the angle between the polarization and particle's extraordinary axis so as to maintain a constant torque.[83,99b] A second, passive approach to applying a constant torque that does not require active feedback is to spin the polarization so fast that the particle can no longer follow. As the polarization spins over the particle, the particle scans the potential and over the course of one revolution the particle experiences a positive and a negative torque. As the polarization is rotated more rapidly, the average torque on the particle approaches zero[114] (**Figure 6d**, point iii). This time-averaged torque clamp becomes more accurate as the timescale of polarization rotation relative to the response time of the particle decreases.

Lastly, we discuss the operation of circularly polarized optical torque tweezers. On the input side, their implementation is very straightforward, as circular polarization can be imposed onto a linearly polarized Gaussian beam simply by passing it through a $\lambda/4$ waveplate oriented at 45° with respect to the input polarization (**Figure 6f.iii**). Rotation of this $\lambda/4$ waveplate away from the 45° orientation changes the ellipticity of the polarization (changing ϕ in **Figure 6a**) This approach has been used to control the average torque transferred to the particle.[105b] As in linearly polarized optical torque tweezers, the transferred torque equals[105a] $\Gamma = \left(\sigma_{z,in} - \sigma_{z,out}\right)P/\omega$. For the case of circularly polarized optical torque tweezers, $\sigma_{z,in}$ equals either +1 or -1. The $\sigma_{z,out}$ will also be constant, because the torque transfer is independent of θ (**Figure 6a**, red line) provided that laser beam wavelength, power, particle size and birefringence are constant. The circularly polarized optical torque tweezers thus provides a third means to operate a torque clamp. This torque clamp is most directly comparable to the force clamp provided by magnetic tweezers (**Section 2**). The magnitude of the optical torque can be adjusted by manipulation of the input power of the beam, since the torque is linear in the power. This, however, raises a problem, because the translational trapping is also proportional to the power and a decrease in optical torque thus also means weaker trapping. A way of circumventing this issue is the use of two incoherent circularly polarized beams that are superimposed in a single trap. Changing the relative power of the two beams while keeping the total power of the trap constant allows to adjust the torque without affecting the translational trapping.[115]

The circularly polarized optical torque tweezers can be calibrated to measure the orientation of the trapped particle. The polarization ellipse at the output of the trap has a constant ellipticity, since $\sigma_{z,out}$ is constant, but its orientation changes as the major axis of the polarization ellipse has a fixed angle with respect to the extraordinary axis of the particle. The orientation of this polarization ellipse can be measured by passing the output beam through a linear polarizer, and measuring the resulting power. Fitting the temporal power signal to the expression $P_m = \{1 + (1 - |\sigma_{z\,out}|)\cos 2\Omega t\}P/2$ (where P is the maximal power) then yields Ω, the rotation rate of the particle relative to the linear polarizer.[105a] Alternatively, if the particle is slowly rotating or not rotating at all, rotation of the polarizer itself yields the same signal and reports on the angular orientation alone, as shown in **Figure 6g** for two values of $\sigma_{z,out}$. An equivalent detection system for deducing the orientation of the trapped particle comprises a polarizing beam splitter and two photodiodes[99a] (**Figure 6f.iv**). A rotatable $\lambda/2$ waveplate can be added to rotate the polarization ellipse. This detection system basically measures the signal twice; the two orthogonal signals are out of phase with one another and their sum should equal a constant total power.

4.7 Brief comparison of linearly polarized optical torque tweezers and magnetic torque tweezers. Before proceeding to the applications of torque spectroscopy (**Section 5**), we close this section on optical torque spectroscopy by providing a brief comparison of the optical torque tweezers that make use of spin angular momentum

with magnetic torque tweezers (**Section 3.2**). These two techniques are similar in the sense that in both a dipole tends to align with an external field (E- or B-field, respectively), and hence both are angular clamps. Which one of these techniques is best used for a given biophysical experiment will depend on numerous factors, including general considerations such as the sensitivity of the sample to light (a general consideration that applies to the use of all types of optical tweezers), but also factors that are specific to torque application or measurement, such as the desired speed of rotation, the sensitivity with which torque needs to be measured, the number of biological specimens that require simultaneously readout of torque, etc. For these latter considerations, we can make concrete comparisons. First, the speed of particle rotation is typically higher in spin-based optical torque tweezers than in conventional MT (or their MTT or eMTT cousins), as in the former the ultimate speed limit is provided by the speed at which the light polarization can be rotated, which may be as high as 1 MHz using currently available electro-optic modulators;[99b] conversely, in the MT rotation is frequently carried out by mechanical rotation of a shaft to which magnets are attached,[45c] which may limits speeds to approximately 20 Hz or less, in the case of MTT. Second, in the spin-based optical torque tweezers, detection of the polarization state of the transmitted light provides a direct measure of the optical torque exerted on the trapped particle (**Figure 5f(ii)**); in the MTT or the eMTT, however, the detectors report on angular shifts (**Figure 3**) which must be multiplied with the local rotational trap stiffness (**Section 3.2**) in order to yield the applied torque. Third, optical tweezers typically employ faster detectors (e.g. photodiodes or position-sensitive detectors

capable of acquiring at 100 kHz – 0.5 MHz rates[70i]), whereas the video-based tracking preferred in magnetic tweezers limits the acquisition rates[45c] to ~100 Hz. Interestingly, in recent years, the introduction of CMOS-based cameras capable of tracking at ~ 10 kHz has started to narrow this gap.[86d,116] Of course, these acquisition rates must always be evaluated in comparison to the actual bandwidth of the system, which is dependent on the stiffness and drag coefficient of the particle employed as a force/torque transducer (**Section 3.4**). For measurements relying on DNA tethers, the characteristic times for rotational motion and torque are generally considerably longer (corresponding to lower bandwidth) compared to the characteristic times for linear motion and force measurements.[46b] Last, there is a clear distinction in the multiplexing capability of spin-based optical torque tweezers versus magnetic torque tweezers. Whereas OT are typically limited to torque detection on a single particle given the preference for individual laser foci in high-resolution optical traps (as opposed to employing time-shared optical traps[117]), MT are capable to monitoring the torques imposed by numerous distinct magnetic beads.[60b] Variations of the local magnetic field over the span of larger samples do not necessarily impose a limitation, since the attendant variations in torsional trap stiffness may simply be calibrated (**Section 3.2**). This facility, together with the use of commercially available super-paramagnetic beads for use in (e)MTT, render the magnetic approaches more suitable for rapid screening of biophysical phenomena or responses, whereas the optical approach permits a more complete characterization of the attendant temporal response.

5. RECENT APPLICATIONS OF SINGLE–MOLECULE TORQUE MEASUREMENTS TO BIOLOGICAL SYSTEMS

In this section, we highlight recent applications of torque spectroscopy. First, we show how the magnetic torque tweezers and the rotor-bead based assay have contributed to our understanding of the mechanics of nucleic acids, in particular DNA. Second, we show how the magnetic torque tweezers, freely-orbiting magnetic tweezers, and the optical torque tweezers have been used to examine DNA-protein interactions relevant to DNA repair and to transcription. Lastly, we show how the use of drag-based methods and magnetic tweezers has recently enhanced our understanding of the operation of the bacterial flagellar motor and the F_0F_1-ATPase, respectively.

5.1. Measurements of DNA torsional properties. Using single-molecule techniques, it has been possible to rigorously map out the mechanical properties of many important biopolymers.[118] Such mechanical properties include the elastic response to bending, stretching, and twisting deformations, which can be characterized by the bending persistence length A, the stretch stiffness S, the torsional persistence length C (**Section 3**), and the twist-stretch coupling D. For the standard B-form helix of double-stranded DNA (dsDNA) in particular (**Figure 1a**), many of its mechanical properties and its structural transitions have been mapped out, primarily using magnetic and optical tweezers;[56a,56c,118-119] standard A-form double-stranded RNA has recently been characterized similarly.[48,120] Quantitative measurement of the torque response of DNA has followed primarily from experiments conducted using magnetic torque tweezers,[59c]

the rotor-bead assay,[63] and the optical torque tweezers,[121] of which several examples are provided below. The collective use of these single-molecule techniques has provided us with a comprehensive view of the force-torque phase diagram of dsDNA[56c,118-119,121b,122] (**Figure 7e**) and dsRNA[48] (**Figure 7f**).

To illustrate a concrete example of how torque spectroscopy can be performed on bare DNA, we detail an MTT experiment. Starting with a torsionally relaxed molecule (corresponding to zero turns in **Figure 7a-d**), the tether extension remains initially approximately constant upon overwinding (corresponding to increasing linking number), as was also observed in the original MT experiments capable of controlling the rotation of the magnetic beads.[45a] In an MTT measurement, one simultaneously observes that the shift in the mean angular signal decreases linearly with increasing number of turns[59c,60a,84] (**Figure 7b**). The shift in the mean angle (**Figure 7c**) can be directly converted to torque (**Figure 7d**) because the stiffness of the torsional trap is independent of the applied number of turns (**Figure 7a**). The effective twist persistence length, C, of DNA can be determined from a fit to the torque data in the region in which the torque builds up linearly with added turns as the torque after N turns equals $2\pi N k_B T C / L_C$, in which L_C is the contour length of DNA. We note that the effective twist-persistence length depends on force and saturates[59c] to 103 ± 5 nm at forces exceeding ~ 4 pN. For the data shown, acquired at a force of 3 pN, the fit yields C_{DNA} ~ 80 nm. As we continued to apply positive turns, the build-up in torsional strain continues until a critical twist density is reached at which the molecule buckled to form plectonemic supercoils[45a] (**Figure 7c**). Beyond this transition, the torque can be

observed to remain constant at Γ_b. The application of negative turns to torsionally relaxed DNA at the applied force shown here ($F > 1$ pN) shows that the tether extension remains approximately constant upon underwinding (**Figure 7c**). The corresponding angle (**Figure 7b**) and torque signals (**Figure 7d**) indicate that initially a similar build-up in torsional strain occurs, until a critical torque Γ_{denat} = −10 ± 1 pN·nm is reached. This asymmetric response of DNA to rotation under this applied force is attributed to local melting (or denaturation) of the double helix,[123] with the MTT reporting on the exact value of the corresponding denaturation torque. At forces above 6 pN, DNA no longer forms plectonemic supercoils upon overwinding but instead undergoes a transition from supercoiled B-DNA to P-DNA (**Figure 7e**), a structurally distinct form of DNA in which the bases are thought to splay outwards from the center of the helix.[124]

Similar approaches have also been employed in order to study specific DNA sequences or constructs. For example, the rotor-bead assay (**Section 2**) has been used to investigate Z-DNA, which is a left-handed helical form of DNA[125] that is favored for sequences that consist of alternating purines and pyrimidines. While under typical physiological conditions Z-DNA is typically less stable than B-DNA, its formation is favored under high ionic strength or negative supercoiling.[125c,126] To investigate the structure of Z-DNA using single-molecule techniques, short guanine/cytosine (GC) repeats have been inserted into longer DNA tethers.[64,127] The behavior of these repeats upon negative supercoiling could then be specifically investigated, either using MT

coupled with fluorescence readout in which the behavior of a pair of fluorescent dyes close to the GC repeat could be monitored,[127] or using the rotor-bead assay in which the angular coordinates of the rotor bead reported on the local torque.[64] A high-resolution version of this experiment, in which both the angular position of the magnetic bead and the angular position of the rotor bead are monitored,[64a] is shown in **Figure 7g**. The corresponding torque read-out is shown in **Figure 7h**. We note that the response of this DNA molecule to applied rotations shows two, rather than one, linear response regions. Here, the reduced slope observed at negative supercoiling[64a] is indicative of the formation of left-handed Z-DNA. As expected, this type of approach can be used to sensitively investigate the torsional response of numerous specific sequences. The same types of techniques can also be employed in the area of DNA nanotechnology, where developments such as those of DNA origami[128] have highlighted the utility of DNA as a construction material at the nanometer-scale.[129] The ability to fabricate DNA boxes,[130] tubing,[131] and other three-dimensional objects[132] and their dreamed-of use as a building material has sparked an interest in the measurement of the mechanical properties of these man-made DNA-based molecular constructs. A first step in this direction was the measurement of the torsional persistence length of four- and six-helix bundles, for which values of $C_{four-helix}$ = 390 $\pm$ 30 nm and $C_{six-helix}$ = 530 $\pm$ 20 nm were obtained (**Figure 7i,j**). As expected, these structures displayed an enhanced torsional stiffness compared to that of a single DNA helix alone.[67]

5.2. Measurements of DNA-protein interactions. With an understanding of the mechanical properties of DNA in hand, the techniques of torque spectroscopy can be

used in order to study DNA-protein interactions (**Figure 8**). An example of how FOMT and MTT can be used together to report on the assembly of nucleoprotein filaments is shown in **Figure 8a,b**. Here, the binding of RAD51 and RecA proteins, respectively, to double-stranded DNA is monitored. Both proteins are known to both lengthen and unwind DNA as they form nucleoprotein filaments.[59d,133] The dynamics of this process can be measured using FOMT, which reports on both the length increase of the DNA-tether determined from the beads' z-position and the unwinding angle θ of the DNA, where the latter is determined by tracking the rotation angle about the DNA-tether axis (with the rotation angle being determined by converting the tracked (x, y)-position to angle,[28b,68] as described in **Section 3**). For example, the blue data in **Figure 8a** show how the addition of relatively high RAD51 concentrations (typically hundreds of nM) results in continuous assembly (marked by an approximately linear increase in the tether length with time and a concomitant unwinding of the tether) until completion is reached (after $\approx$ 1000 s). From these experiments, the unwinding angle per RAD51 monomer can be determined[59d] to be 46° ± 2°, by using the total length change and the known change in length per RAD51 monomer to compute the number of bound monomers and dividing the total unwinding angle by this result. A similar behavior is observed for RecA nucleoprotein assembly on dsDNA[28b] (**Figure 8a,** red data), which yields an unwinding angle per RecA monomer of 44.7° ± 1.4°, in good agreement with the value (45.8°) determined from crystallography.[133]

Following assembly, the torsional stiffness of the resulting nucleoprotein filaments can be measured using the MTT (**Figure 8b**). For both RAD51 filaments and RecA filaments, we initially observe a linear response of the torque with the applied number of turns (**Figure 8b,** blue and red data, respectively; zero turns corresponds to the torsionally relaxed filaments). The torsional persistence length C of these filaments can be determined from linear fits to the linear response regime of the torque vs. turn response (**Figure 8b,** blue and red solid lines), as in the case of bare DNA (**Figure 7b,d**) or DNA origami constructs (**Figure 7j**). Interestingly, the torsional stiffness of the RAD51 filament is found to exceed that of its RecA counterpart by a factor of three (C_{Rad51} = 504 ± 57 nm, $C_{RecA} = 173 \pm 5$ nm), even when the two filaments were assembled under similar conditions (Mg^{2+}-AMPPNP for RAD51, Mg^{2+}-ATPγS for RecA, both filaments under a force of 3.5 pN). As the same trend is not observed in the case of the bending persistence length (~300 nm for RAD51 filaments,[59d,134] ~600 nm for RecA filaments[135]), this illustrates that a filament's bending stiffness and its torsional stiffness are *a priori* independent quantities. For both nucleoprotein filaments, upon further over- or under-winding, the torque eventually saturates (**Figure 8b**) and remains constant at values close to those previously observed for structural transitions of B-form DNA (melting upon underwinding and the B-to-P-form transition upon overwinding,[121a] **Figure 7d,e**). This suggests that sufficiently large torsional stresses can locally disrupt the nucleoprotein filaments, and that the DNA within the filament can locally melt or adopt the P-form DNA configuration.

As mentioned in **Section 1**, the ability of DNA to store torque has implications for the motor proteins that either generate this torque or are confronted with it. While it has been known previously that bacterial RNA polymerase will stall when it needs to apply forces in excess of 25 pN,[17] a measurement of the value of the torque that induced stalling by RNA polymerase was not known until very recently. To measure this stall torque, surface-bound *E. coli* RNAP performed transcription on a DNA that was tethered and rotationally constrained in an angular optical trap[5] (**Figure 8c**). Transcription by *E. coli* RNAP resulted in the generation of upstream (-) supercoiling or downstream (+) supercoiling in the tethered DNA (depending on the orientation of its promoter). While in principle the accompanying torque could be read out optically (**Figure 2n**), in these experiments the torque signal was too noisy for use in direct measurements of RNAP dynamics. Instead, therefore, the torque was inferred indirectly from the measured force and extension of the torsionally constrained DNA. When a critical torque was reached, the polymerase was stalled. The mean absolute value of the stall torque was 11 pN·nm, independent of the sign of the supercoiling. Interestingly, this stall torque is just sufficient to melt negatively supercoiled DNA.

5.3. Measurements of membrane-based molecular machines. Lastly, we discuss two applications of torque spectroscopy to membrane-based molecular machines. One such machine, the ATP synthase (also known as the F_0F_1-ATPase), was briefly discussed in **Section 1** (**Figure 1d,e**). This remarkably coupled machinery consists of the F_0 subunit which is embedded in the membrane together with the F_1 subunit, which is positioned

directly beneath it. The reconstitution of active F_1 has facilitated in-depth studies of this motor[136] (reconstitution of the membrane-bound F_0 being far more difficult to achieve). Already in the 1980s, it was suggested by several scientists that this motor complex should rotate.[137] Crystallographic data subsequently confirmed this supposition,[138] as did spectroscopic approaches.[139] Single-molecule fluorescence experiments, in which a fluorescently-labeled actin filament was added to the γ subunit, made direct visual observation of the rotary motion possible for the first time[29] (**Figure 2b**). Analysis of the pausing in the angular coordinate could then already report on the different states visited by the motor, and revealed that the γ subunit that forms the rotary shaft of the F_1 motor primarily advances in three 120° steps,[29] powered by the three catalytic β subunits,[138] with substeps of 40° and 80° in size.[30]

However, for the full investigation of the mechano-chemical cycle of the F_1 motor, the addition of tweezer-based methods has proved very fruitful. Here, the standard approach is to attach to the γ subunit a magnetic bead, which can then be manipulated via external magnetic fields: for example, an arrangement of four electromagnets placed at right angles to one another while appropriately phase-shifted currents were passed through them could be used to rotate the magnetic bead, and hence the γ subunit. In this way, it was possible to drive the motor mechanically (instead of using a proton gradient) and force the synthesis of ATP,[140] which indicates that the catalytic state of the three β subunits is very tightly coupled to the rotation of the γ subunit. A different use of the same technique is illustrated in **Figure 9a**, in which one first observes pausing of

the F_1 motor and then, during the pausing, uses permanent magnets to displace the F_1 motor from its stable point to nearby locations within its rotary cycle.[13,141] After a well-defined time interval, the motor is subsequently released, while it is observed whether it can advance along its rotary cycle (designated as Forward 'on' in the upper righthand panel of **Figure 9a**) or whether it reverts back to its earlier stable point (designated as Return 'off' in the upper righthand panel of **Figure 9a**). Such experiments allow one to determine at which points in the angular cycle the steps of torque generation are mostly likely to occur. For example, in the lower panels of **Figure 9a**, the γ subunit of the F_1 motor is displaced by +30° (left) or -30° (right) from a stable pause position to probe for ATP binding and torque generation. When displaced by +30°, the F_1 motor was observed to move on to the subsequent angular position (displaying Forward 'on' behavior), but when it was displaced by -30°, it first returned to the original angular position (displaying Return 'off' behavior). These types of experiments permit one to map out, as a function of angle, the probability of ATP binding and the corresponding energy landscape. Corresponding experiments probing the angular mapping of ATP hydrolysis additionally report on the coupling between mechanical motion and chemical activity can be mapped out,[142] allowing for a complete dissection of F_1's mechanochemical cycle.

Interestingly, similar machines are also used in bacterial propulsion. Indeed, how to efficiently advance in liquid appears to have been settled at the micro-meter scale of swimming bacteria billions of years ago, as most swimming bacteria are powered by

rotary engines, known as the bacterial flagellar motors.[143] At very different length scales, it has also occupied naval engineers (see **Box 3**). Bacterial flagellar motors are complicated and tightly regulated machines that have an overall size of ~45-50 nm and typically consist of over 20 protein species. They are maintained within the cell membrane and employ membrane-anchored stators to drive a rotary shaft.[144] The generated power is transmitted to the filament via a structure known as the hook, which consists of a single protein called flagellin and is 20 nm in diameter,[143b] resulting in rotation of the flagellum at ~100 Hz in either the clockwise or counterclockwise direction.[38c] Depending on the type of bacterium, either a single or multiple of these flagella are employed in cellular swimming.

Box 3. Propulsion in liquid at macroscopic and microscopic scales. In the mid-19th century, it was becoming obvious to naval engineers that steam engines were superior to sails, in particular in naval combat. However, it was hotly debated how to best transmit the power: using paddle wheels, the dominant technology at the time, or rotary propeller screws? Eventually, British admiralty ordered a tug-of-war and the superiority of the rotary propeller was settled once and for all when, under full steam, the screw-driven *HMS Rattler* pulled a paddle wheeler backward with 2 knots. At the micro-meter scale of swimming bacteria, the rotary motor is also used for propulsion, as many bacteria employ a rotary flagellar motor to apply torque to their flagella and advance.[143] The resulting rotary motion makes it possible for micron-sized bacteria to advance in fluid, overcoming the challenges posed by the low Reynolds number

environment. Similar principles are also employed by many single-cellular eukaryotes to propel themselves through fluid.[143a]

Over the past few decades, numerous biophysical techniques have been used to probe the operation of the bacterial flagellar motor in order to understand its mechanism of torque generation. Early experiments performed in the 1970s utilized cells that were tethered to a surface by filaments, allowing rotation of the cell body, driven by the motor, to be observed.[23a,145] While other methods have been employed, e.g. light scattering, darkfield microscopy, differential interference microscopy, or fluorescence microscopy, the most widely-used approach to study flagellar rotation has been through the use of sub-micron polystyrene beads attached to truncated flagellar filaments of immobilised cells. Motion of these beads, and hence of the flagellum, can be monitored using back focal plane interferometry[25] or high-speed fluorescence microscopy.[25c,38d] Such drag-based methods (**Figure 2b**) have made it possible to map out the torque exerted by the flagellar motor as a function of the motor's angular velocity, which provides an excellent test of models for the flagellar motor's underlying mechanochemistry (for recent modeling studies, see[146]). This experimentally-determined torque-speed curve reveals that the torque exerted by the *E. coli* flagellar motor is approximately constant up to speeds of nearly 200 Hz, and that subsequently the torque exerted by the motor declines approximately linearly with speed, crossing the 0-torque line at ~300 Hz. Estimates of the torque generated in the low-speed regime range from about 2700 pN·nm to 4600 pN·nm, depending on the experimental

approach employed.[38c]

A powerful approach for the study of the bacterial flagellar motor comes from so-called "resurrection experiments", in which the expression of the torque-generating stators is placed under induction control.[147] In such an experiment, it is possible to monitor the changes in the angular velocity of a sub-micron polystyrene bead that accompany the insertion of each subsequent stator into the motor complex. Interestingly, it has been observed that the speed increase per stator increase depends on the torque load[25a,38d,148] (**Figure 9b**). For instance, at high loads (generated by 1 μm beads; top panel), the speed increases linearly with the number of stators; at intermediate loads (generated by 0.3 μm beads; center panel), the speed increases in a nonlinear fashion with the number of stators; and at low loads (generated by 60 nm gold beads; bottom panel), the speed hardly increases with increased numbers of stators. This has been interpreted as being the consequence of a high duty ratio, in which each stator contacts the rotor for an extensive period of time. When the motor is spinning quickly under conditions of low load, the addition of subsequent stators does not increase the angular velocity due to a lack of sufficient time for intervention or even a hampering of ongoing motor activity.

To probe the behavior of the bacterial flagellar motor in regimes in which it rotates backwards at negative speeds or forwards at positive speeds that exceed the speeds achieved under zero load, additional manipulation is required and can be achieved by

e.g. electrorotation[38c] (**Figure 2d**). Electrorotation measurements[38d] have indicated that the plateau of constant torque extends out to backwards speeds of about 100 Hz. However, electrorotation experiments suffer from a difficulty in the exact calibration of the applied torques, and hence further developments of techniques to probe the torque-speed curve remain of great interest.

6. OUTLOOK

We have seen in this Review that the number of techniques that can report on and manipulate the angular motion and apply torque to biological systems has increased steadily in recent years, and that these techniques have been harnessed to great effect to investigate a variety of biological systems. Future developments of both the torque transducers and the instruments that manipulate them should provide improvements in angular sensitivity, torque sensitivity, and temporal resolution, making it possible to probe the workings of the enzymes and molecular machines that are sensitive to torque at unprecedented resolution. Additionally, improvements in the ability to target torque transducers to particular locations within rotary machines should make it possible to understand their underlying mechanics more completely. We also expect that it will become possible to transfer some of these techniques into the intracellular environment. This will make it possible to probe rotary machines *in situ* and contribute to our overall understanding of cellular function.

Box 4. GLOSSARY OF SELECTED TERMS

Birefringence

The property of a material that its index of refraction varies along different coordinates for different polarization states. As a result, light will interact differently along the material's axes, an effect that is utilized in optical torque tweezers.

Crystal anisotropy

A material property found in crystalline materials in which the binding forces between atoms in the crystal vary between the crystal axes. These differences in binding forces result in distinct propagation velocities (and hence the indices of refraction) along the crystal axes, resulting in birefringence.

Index of refraction

A material property equal to the ratio of the speed of light in vacuum to the speed of light in the material.

Magnetic tweezers

A single-molecule technique in which magnets are used to apply forces and torques to biological macromolecules that are tethered between a surface and magnetic beads.

Magnetic torque tweezers

A variant of the magnetic tweezers that provides a direct read-out of the torque stored in a tethered biological molecule.

Freely-orbiting magnetic tweezers

A variant of the magnetic tweezers that does not constrain the free-rotation of the magnetic bead about the molecular tether axis and provides a direct read-out of

changes in the angular coordinate of tethered biological systems, while maintaining the ability of apply stretching forces.

Optical tweezers

A single-molecule technique in which a focused laser beam is used to apply forces to dielectric beads to which biological molecules can be tethered.

Optical torque tweezers (also referred to as **optical torque wrench)**

A variant of the optical tweezers that can provides a direct read-out of the torque stored in a tethered biological molecule.

Poynting vector

*The cross product (1/μ)**E** x **B**, where **E** and **B** are the electric and magnetic components of an electromagnetic wave, respectively. For a traveling electromagnetic wave, the Poynting vector points in the direction of wave propagation.*

Rotor-bead assay

A single-molecule technique in which an angular transducer is incorporated (internally) into a tethered biological molecule, allowing changes in its angular coordinate to be monitored, typically in the presence of an applied force.

Shape anisotropy

A geometric property of microscopic particles (sized order of or less than λ) composed of inherently isotropic materials, in which differences in the particle's dimensions along its different axes lead to differences in polarizability, hence in birefringence.

Figure and Table Captions

Figure 1. Twist and torque in biological systems. (a) Rendering of the DNA double helix. The figure was drawn from protein data bank entry 2BNA[22] using VMD.[149] **(b)** The linking number (Lk) is a quantitative descriptor of DNA topology that includes the number of times the helix winds around its central axis and the number of times the helix crosses itself. ''Twist'' (Tw) is the number of helical turns in the duplex DNA. Alternatively, ''writhe'' (Wr) occurs when the DNA helix buckles into loop-like structures called plectonemic supercoils, or when the DNA wraps around proteins complexes, such as nucleosomes. Lk is the sum of Tw and Wr (Lk = Tw + Wr). As illustrated here, a decrease in linking number of -4 could be accommodated by a pure change in Wr with the formation of 4 plectonemic supercoils. Reprinted with permission from Ref.[9d] Copyright 2010 Cell Press. **(c)** Consequences of the helical nature of DNA for RNA polymerase (brown oval-shaped object), which unwinds DNA as it proceeds to generate an RNA transcript (shown in dark blue). If RNA polymerase cannot rotate about the DNA axis – which may occur when ribosomal proteins (yellow) bind to the nascent RNA and synthesize membrane-binding proteins, as illustrated, then the downstream DNA will be forced to rotate. In the presence of locally constrained DNA extremities, this will result in the introduction of supercoils in the DNA. Reprinted with permission from Ref.[9d] Copyright 2010 Cell Press. **(d)-(e)** Example of a rotational engine across cell membranes: F_0F_1-ATPase, which generates ATP. F_0F_1-ATPase consists of two connected molecular motors: F_0 (collection of brown subunits), which is largely embedded in the membrane, and F_1 (collection of green subunits), which protrudes from the membrane. When the

proton-motive force that powers F_0 is sufficiently large, the torque generated by F_0 exceeds that of F_1, and the resulting clockwise rotation of the rotor drives ATP synthesis as shown in **(d)**. When the proton-motive force is low, ATP hydrolysis can result in excess torque generated by F_1 over F_0, and the resulting counterclockwise rotation of the rotor pumps protons in the reverse direction resulting in restoration of the proton-motive force, depicted in **(e)**. Data in (d), (e) adapted with permission from Ref.[13] Copyright 2013 Federation of the European Biochemical Societies.

Figure 2. Overview of single-molecule twist and torque measurement approaches. (a)-(c) Viscous drag-based methods. **(a)** An *E. coli* cell body (green) is attached by its flagellum (black) to a glass slide (blue). The rotation of the cell body is used to read out the operation of the bacterial flagellar motor (red). **(b)** The rotation of an actin filament (assembly of purple spherical monomers) artificially tethered to the γ-subunit (yellow) of the F_1 motor is used to read out the operation of this motor. **(c)** The rotation of a bead-pair (brown) tethered to DNA (black) is used to read out changes in DNA twist. **(d)** The application of torque via the interaction of electric fields generated by two pairs of electrodes (grey) with a polarized object, in this case an *E. coli* cell body (green), so-called electrorotation. **(e)** Rotor-bead assay using optical tweezers.[28a] The position of the rotor bead (green), determined via fluorescence excitation or light scattering, provides the angular readout. **(f-j)** Different types of magnetic tweezers configurations, specifically **(f)** Conventional magnetic tweezers in which a pair of magnets is employed to apply (but not measure) torque. **(g)** Magnetic torque tweezers,[59c,60a] in which a

cylindrical magnet aided by a side-magnet is used, together with a form of angular readout (**Section 3**), to apply and measure torque. In this illustration, angular readout proceeds by tracking the position of a marker bead (green) attached to the magnetic bead. **(h)** Electromagnetic torque tweezers in which a cylindrical magnet aided by a pair of Helmholtz coils is used, together with a form of angular readout (**Section 3**), to apply and measure torque.[68] **(i)** Freely-orbiting magnetic tweezers employ a well-aligned cylindrical magnet, together with an angular readout, to report on changes in DNA twist.[28b] **(j)** Rotor-bead assay using magnetic tweezers. The position of the rotor bead (green sphere), determined via fluorescence excitation or light scattering, provides the angular readout. **(k-n)** Different types of optical torque tweezers configurations, specifically **(k)** Optical torque tweezers that rely on the movement of a lever arm. **(l)** Optical torque tweezers that operate using the transfer of orbital angular momentum. **(m)** Optical tweezers that operate using the transfer of spin angular momentum via a disk-shaped particle (shape birefringence). **(n)** Optical tweezers that operate using the transfer of spin angular momentum via a quartz cylinder (material birefringence).

Figure 3. Principle of torque measurement in magnetic torque tweezers. (a) Schematic showing the principle of the torque measurement. After over- (or under-)winding the DNA tether by *N* turns, the DNA exerts a restoring torque on the bead that leads to a shift in the equilibrium angular position from θ_0 to θ_N. **(b)** Example of angle traces used to measure torque: angular fluctuations of a bead tethered to a torsionally relaxed 7.9 kbp DNA molecule at a stretching force of ≈ 3.5 pN before (blue) and after (dark red)

introducing 40 turns. The standard deviation of the fluctuations is $\sigma_\theta \approx 9° \approx 0.16$ rad for both traces, corresponding to a angular trap stiffness of $k_\theta = k_B T/\sigma_\theta^2 \approx 160$ pN·nm/rad (Equation 1). The shift in the mean after rotating 40 turns is $\langle \theta_N - \theta_0 \rangle \approx -8° \approx -0.14$ rad; multiplying this shift by the rotational trap stiffness gives the restoring torque (Equation 6) to be $\Gamma_{DNA} \approx 23$ pN·nm; this is close to the buckling torque of DNA at this stretching force. Panels adapted with permission from Ref.[59c] Copyright 2010 Nature Publishing Group.

Figure 4. Angular accuracy and confinement for different magnetic tweezers configurations. (a) Overview of angular fluctuations in different magnetic tweezers configurations. The angular fluctuations are largest in the FOMT (orange curve); to see the smallest angular fluctuations, an inset is provided. The traces for a stuck bead (black), a bead held in conventional MT (blue), and for a bead in the MTT (dark red) were recorded using 2.8 µm diameter M270 beads with a 1 µm diameter non-magnetic marker bead attached, employing a 7.9 kbp DNA tether at a stretching force of 3.5 pN. The trace for a bead held in the FOMT (orange) was obtained using a 0.7 µm diameter bead and a 3.4 kbp DNA tether at a stretching force of 1 pN. **(b)**-**(e)** Histograms corresponding to the angular fluctuations in the different magnetic tweezers configurations shown in (a). Note the ten-fold difference in the range of the x-axis with each subsequent panel. **(f)** Determination of the characteristic time scale $\tau_C = \gamma_\theta/k_\theta$ for the different magnetic tweezers configurations shown in (a) by fitting an exponential decay to the temporal autocorrelation data. The characteristic times determined from

the fits are τ_C < 0.1 s, ~ 0.9 s, and ~ 7 s for the MT, MTT, and FOMT traces, respectively. **(g)** Power spectra of the angular fluctuations traces. Fitting the power spectral density of the angular fluctuations to a Lorentzian function (Equation 12) provides an alternative method to determining the characteristic time scale of the fluctuations. From the fits, we find $\tau_C = 1/(2\,\pi f_C)$ ~ 0.04 s, 0.8 s, and 7 s for the MT, MTT, and FOMT traces, respectively (f_C values are indicated in the figure). Note that for plots and analysis in panels (e)-(g) more points were used than are shown in the FOMT trace in panel (a).

Figure 5. Birefringence and birefringent particles for optical application and detection of torque. (a) Decomposition of a linearly polarized wave (red) into two orthogonal linearly polarized components (blue and purple). **(b)** Index ellipsoids for an isotropic material with equal indices of refraction along its three axes $n_1 = n_2 = n_3$. A negative uniaxial birefringent material with one index of refraction smaller than the other two indices $n_e < n_o = n_o$; a positive uniaxial birefringent material with one index of refraction larger than the other two indices $n_o = n_o < n_e$; and a biaxial material with three different indices of refraction along its axes $n_1 < n_2 < n_3$. **(c)** Induced phase delay in a birefringent material. Two orthogonal linear components (blue and purple) oscillate in phase. Between the grey interfaces the orthogonal components travel at different velocities over a distance d, hence the nodes no longer coincide. Upon exiting the second interface the two orthogonal components are 180 degrees out of phase. Here the nodes coincide again, but the purple component now oscillates in opposite direction with respect to the blue component. **(d)** Electric susceptibility χ. The wave's electric

field vector E induces an electric dipole moment p. In a birefringent material the susceptibility along the extraordinary axis χ_e is different from the susceptibility along the ordinary axis χ_o and therefore the induced dipole p is not collinear with the external field E. The misalignment of p and E generates the torque Γ. **(e)** Example of crystal anisotropy: vaterite. The SEM image shown is of an uncoated vaterite sphere. Reprinted with permission from Figure 1b in Ref.[109b] Copyright 2009 American Chemical Society**. (f)** Example of crystal anisotropy: quartz. The SEM image shown is of a nanofabricated quartz particle. Reprinted with permission from Figure 3g in Ref.[110b] Copyright 2011 American Chemical Society. **(g)** Alignment of a cylindrical particle in a linearly polarized trap. A large particle (with respect to the beam size) such as the quartz particle shown in **(f)**, will align its extended axis with the beam axis as shown. **(h)** Example of shape anisotropy: disks. Sequence of bright field images of a disk rotated in an optical trap viewed from below. Image from Figure 15.5 reprinted with permission from Ref.[99b] Copyright 2010 Elsevier. **(i)** Example of shape anisotropy: nanorods. The SEM image shown is of gold nanorods. Image from Figure 1b reprinted with permission from Ref.[94a] Copyright 2011 American Physical Society. **(j)** Alignment of a cylindrical particle in a linearly polarized trap. A small particle (with respect to the beam) such as the smaller gold nanorod in **(i)** will align with the linear polarization as shown.

Figure 6. Application and detection of torque using optical tweezers. (a). The optical torque that can be transferred to a birefringent material as a function of the angle θ between polarization and extraordinary axis of the material for different degrees of

polarization ellipticity ϕ. The phase delay, Δ_p, is set to 1, where $\Delta_p = \pi/2$ would apply for a $\lambda/4$ wave plate. The solid black dots indicate stable trapping positions (valleys in the potential), where the torque is zero and where small angular deviations result in a torque forcing the system back to this position, as indicated by the arrows. The open circles indicate unstable positions (peaks in the potential), where the torque is also zero, but small angular deviations now result in a torque away from this position, as indicated by the arrows. **(b)** The optical torque that can be transferred to a birefringent material as a function of the thickness of the material d for linear polarization ($\phi = 0, \theta = -45°$) and circular polarization ($\phi = \pi/4$). **(c)** Torque traces measured during the rotation of a linear polarization. (i-iii) Torque (black) and polarization angle (red) as a function of time for different polarization rotation rates indicated by the red circles in (d). Reprinted with permission from Ref.[112] Copyright 2011 Nature Publishing Group. **(d)** Mean value of the measured torque for different polarization rotation rates. Reprinted with permission from Ref.[112] Copyright 2011 Nature Publishing Group. **(e)** Standard deviation of the measured torque for different polarization rotation rates (dataset different from **c** and **d**). Reprinted with permission from Ref.[113] Copyright 2012 Optical Society of America. **(f)** Schematic for an optical setup to control input polarization and measure output polarization. The following abbreviations are used: EOM – electro-optic modulator; $\lambda/4$ – quarter wave plate; OBJ – objective; $\lambda/2$ – half wave plate; PD – photodiode; PBS – polarizing beam splitter. We highlight four schemes: (i) Generation of a linear polarization with controllable orientation using an EOM and a $\lambda/4$ wave plate. The axes of the EOM should be at $45°$ with respect to the linear input polarization as to

have equal-amplitude components traveling along the axes of the EOM. The EOM will then introduce a voltage-dependent phase shift between these components. The axes of $\lambda/4$ wave plate should be at $45°$ with respect to the axes of the EOM, so the two linear component relayed by the EOM will be mapped into two circular components of opposite handedness. Since both components have equal amplitude, the resulting polarization will be linear and its orientation will depend on the phase shift introduced by the EOM; (ii) Measurement of circular components of the output polarization. The $\lambda/4$ wave plate converts the circular polarization components (below dashed box of (ii)) of the trap output into linear components. Placing the $\lambda/4$ wave plate at $45°$ with respect to the PBS allows the linear components relayed by the $\lambda/4$ wave plate to be split by the PBS. After the PBS, the PDs measure the intensities of the two components; (iii) Generation of a circular input polarization using a $\lambda/4$ wave plate. The axes of the $\lambda/4$ wave plate should be at $45°$ with respect to the linear input polarization to generate a circular polarization; (iv) Measurement of the linear components of the output polarization. The PBS splits the linear polarization components (above dashed box of (iv)) of the trap output and the PDs measure the intensities of the two components. A rotatable $\lambda/2$ wave plate can be used, if the particle inside the trap is stationary (main text). **(g)** Power signal that would theoretically be detected by either one of the photodetectors in **f.iv**, if the input polarization were circular $\sigma_{z,in} = 1$ and the output polarization were either linear $\sigma_{z,out} = 0$ (dotted line) or elliptical $\sigma_{z,out} = 0.6$ (dashed line) for a particle rotating at 4 Hz. The signal oscillates at 8 Hz.

Figure 7. Application of torque spectroscopy to nucleic acids. (a-d) Torque measurement on a 7.9 kbp DNA molecule in PBS buffer held at a stretching force of ~3 pN using the fiducial marker bead based angular tracking protocol. Angular fluctuations as shown in (b) were recorded as a function of the number of applied turns. **(a)** The standard deviation of the angular fluctuations as a function of applied turns. The width of the fluctuations is approximately constant, indicating constant angular trap stiffness. **(b)** The shift in the mean rotation angle as a function of applied turns. Systematic shifts of the mean angle upon over- and underwinding of the DNA are apparent. **(c)** The DNA tether extension as a function of applied turns. This signal is recorded simultaneously with the angular signals in (a), (b). **(d)** The torque exerted by the DNA tether determined from the mean angle shown in (d), see main text. Over- and underwinding around zero turns gives rise to a linear torque vs. turns response of the DNA-tether (fitted grey slopes ion (b) and (d)) that can be used to determine the effective torsional persistence length (C_{DNA} ~ 77 nm for this data set). Further overwinding leads to buckling and formation of plectonemic supercoils (schematically shown in the insets), corresponding to a torque plateau (black line at positive turns in (d) at ~26 pN·nm) and a linear decrease of the tether extension with number of turns (black slope in (c)). Unwinding beyond the linear regime causes the DNA to locally melt (shown in the insets on the left), marked by a torque plateau equal to the melting torque (black line at negative turns in (d) at ~ –11 pN·nm). **(e,f)** Force-torque phase diagram for double-stranded DNA (e) and double-stranded RNA (f) as a function of applied force and torque. Blue and red points connected by solid lines correspond to transitions directly measured;[48,59c] blue

squares are data points from Ref.[121b] Dashed lines correspond to putative transition regions that have not been directly observed. B, B-form DNA; A, A-form dsRNA; −scA/B and +scA/B , negatively and positively supercoiled A-form dsRNA or B-form DNA, respectively. L-DNA/RNA, P-DNA/RNA, and S-DNA/RNA denote the alternative conformations induced by large forces and torques.[48,121b] **(g)** Implementation of the rotor-bead assay in which the angular position of both the upper magnetic bead and the lower non-magnetic rotor bead are monitored. Adapted with permission from Ref.[64a] Copyright 2013 American Physical Society. **(h)** Use of the rotor-bead assay to examine the structural transition from B-DNA to Z-DNA. Reprinted with permission from Ref.[64a] Copyright 2013 American Physical Society. **(i,j)** Use of the MTT to quantify the torsional response of DNA bundles formed using DNA origami. The implementation is shown in **(i)**. Adapted with permission from Ref.[67] Copyright 2011 American Chemical Society. The,results on six-helix (left, data shown at 2.0 pN (red circles) and 3.7 pN (red triangles)) and four-helix (right, data shown at 9 pN (green circles) and 6 pN (green triangles)) DNA bundles are shown in **(j)**. The plots both show the measured torque as a function of the number of applied turns, and indicate that both bundles are substantially stiffer in the torsional coordinate ($C_{six-helix}$ = 530 $\pm$ 20 nm, $C_{four-helix}$ = 390 $\pm$ 30 nm) compared to a single helix of DNA (high-force limit for C estimated at 97 $\pm$ 4 nm under these conditions, see also **Section 3**). Reprinted with permission from Ref.[67] Copyright 2011 American Chemical Society**.**

Figure 8. Application of torque spectroscopy to DNA-protein interactions. In all three panels, the technique employed to perform the measurement is shown at left. **(a)** Use

of the FOMT to measure the formation of RAD51 (blue) and RecA (red) nucleoprotein filaments on dsDNA. As RAD51 (blue) or RecA (red) monomers successively bind to dsDNA, they extend the contour length (top) while unwinding the DNA helix (bottom). Stable assembly was ensured by performing the RAD51 experiments in the presence of Ca^{2+}, which inhibits ATP hydrolysis,[150] and by performing the RecA experiments in the presence of the nonhydrolyzable ATP analog[151] ATP-γS. For the case of RAD51, the contour length increased from 2.74 ± 0.08 μm to 4.04 ± 0.13 μm and a total unwinding by −313 ± 14 turns was observed (mean and SEM of 8 measurements at saturating condition). For the case of RecA, the contour length increased to 4.1 ± 0.1 μm and a total unwinding by − 328 ± 10 turns was observed. **(b)** Use of the MTT to compare the torsional persistence length of bare DNA (grey points), the RAD51 nucleoprotein filament on dsDNA (blue points), and the RecA nucleoprotein filament on dsDNA (red points). For RAD51-dsDNA filaments assembled in the presence of ATP and Ca^{2+}, we found $C_{RAD51} =$ 504 ± 57 nm (mean and SEM from 4 measurements) at a stretching force of 3.5 pN. For RecA, we found $C_{RecA} = 173$ ± 5 nm (mean and SEM from 10 measurements) at the same value of the stretching force. Thus, the torsional persistence length of the RAD51 nucleoprotein filament exceeds that of its RecA counterpart by a factor of three. **(c)** Use of the optical torque wrench to provide RNA polymerase with a rotationally constrained DNA substrate and estimate its stall torque. The green ellipse indicates the RNAP and the green arrow its translocation direction on the DNA. At stage 1 the force on the DNA is clamped at ~0.2 pN and the DNA contains negative plectonemes that are mechanically introduced by rotation of the quartz

cylinder. The torque present in the DNA at any given time is estimated from the measured force and extension.[5] As the RNAP translocates, the extension in basepairs decreases (not shown), but the extension of the DNA in nm increases (top graph) due to the removal of negative plectonemes, and the torque remains constant (bottom graph). At stage 2 the RNAP has neutralized the negative plectonemes and continues to form positive plectonemes in stage 3. Following stage 3 the force clamp is turned off, and the RNAP proceeds until it stalls when the torque built up in the DNA reaches about 11 pN·nm. Reprinted with permission from Ref.[5] Copyright 2013 American Association for the Advancement of Science.

Figure 9. Application of torque spectroscopy to membrane-based machines. (a) (Top) Use of magnet-based manipulation to displace a paused F_1-ATPase from its equilibrium position for ATP binding in order to probe its mechanochemical cycle. Such displacement is effectuated attaching a magnetic bead to the rotor of F_1-ATPase (the γ subunit) and by orienting the magnets to the desired angular position, as shown in the central panel. F_1-ATPase is then stalled in this orientation for a defined period of time. The magnets are then released and subsequent rotation of the rotor is monitored. If ATP binding has occurred, which allows torque to be generated, F_1-ATPase will not return to its original stalled position (as indicated by Forward 'on' in the right panel). If ATP binding has not occurred and torque cannot be generated, F_1-ATPase will return to its original stalled position (as indicated by Return 'off' in the top right panel). (Bottom) In the lefthand panel, the rotor is displaced by +30° for 0.5 s (blue datapoints) from its

paused position (at 1.0 turns) after which it continues along its cycle, indicating that ATP binding has occurred. In the righthand panel, the rotor is displaced by -30° for 5 s (blue datapoints) from its paused position (at 1.33 turns, a position analogous to 1.0 turns) to which it returns afterwards, indicating that ATP binding has not occurred. Reprinted with permission from Ref.[141] Copyright 2012 Nature Publishing Group. **(b)** Monitoring the rotational speed of the bacterial flagellar motor as a function of the number of active stator subunits. The rotational speed is monitored by following the angular motion of a bead tethered to the flagellar motor, whereby the bead decreases in size from the top to the bottom subpanel. When large beads are used (top panel), the load is high and the speed is low, in which case the angular speed is observed to increase with the number of active stator subunits. When small beads are used (bottom panel), the load is low and the speed is high, in which case the angular speed no longer increases with the number of active stator subunits. The center panel represents an intermediate situation in which the angular speed appears to saturate at relatively low numbers of active stator subunits. Reprinted with permission from Ref.[38d] Copyright 2008 Cambridge University Press.

REFERENCES

(1) Watson, J. D.; Crick, F. H. *Nature* **1953**, *171*, 737.

(2) (a) Watson, J. D.; Crick, F. H. *Nature* **1953**, *171*, 964. (b) Liu, L. F.; Wang, J. C. *Proc. Natl. Acad. Sci. U.S.A.* **1987**, *84*, 7024. (c) Cozzarelli, N. R.; Cost, G. J.; Nollmann, M.; Viard, T.; Stray, J. E. *Nat. Rev. Mol. Cell Biol.* **2006**, *7*, 580.

(3) Vologodskii, A. V.; Cozzarelli, N. R. *Annu. Rev. Biophys. Biomol. Struct.* **1994**, *23*, 609.

(4) Borukhov, S.; Nudler, E. *Curr. Opin. Microbiol.* **2003**, *6*, 93.

(5) Ma, J.; Bai, L.; Wang, M. D. *Science* **2013**, *340*, 1580.

(6) (a) Worcel, A.; Strogatz, S.; Riley, D. *Proc. Natl. Acad. Sci. U.S.A.* **1981**, *78*, 1461. (b) Kornberg, R. D. *Annu. Rev. Biochem.* **1977**, *46*, 931. (c) Luger, K.; Mader, A. W.; Richmond, R. K.; Sargent, D. F.; Richmond, T. J. *Nature* **1997**, *389*, 251.

(7) Fudenberg, G.; Mirny, L. A. *Curr. Opin. Genet. Dev.* **2012**, *22*, 115.

(8) (a) Browning, D. F.; Grainger, D. C.; Busby, S. J. *Curr. Opin. Microbiol.* **2010**, *13*, 773. (b) Dillon, S. C.; Dorman, C. J. *Nature Rev. Microbiol.* **2010**, *8*, 185.

(9) (a) Wang, J. C. *Annu. Rev. Biochem.* **1985**, *54*, 665. (b) Wang, J. C. *Q. Rev. Biophys.* **1998**, *31*, 107. (c) Champoux, J. J. *Annu. Rev. Biochem.* **2001**, *70*, 369. (d) Koster, D. A.; Crut, A.; Shuman, S.; Bjornsti, M. A.; Dekker, N. H. *Cell* **2010**, *142*, 519.

(10) Roca, J. *Chromosoma* **2011**, *120*, 323.

(11) (a) Menzel, R.; Gellert, M. *Cell* **1983**, *34*, 105. (b) Lim, H. M.; Lewis, D. E.; Lee, H. J.; Liu, M.; Adhya, S. *Biochemistry* **2003**, *42*, 10718. (c) Hatfield, G. W.; Benham, C. J. *Annu. Rev. Genet.* **2002**, *36*, 175. (d) Travers, A.; Muskhelishvili, G. *Nature Rev. Microbiol.* **2005**, *3*, 157. (e) Vijayan, V.; Zuzow, R.; O'Shea, E. K. *Proc. Natl. Acad. Sci. U.S.A.* **2009**, *106*, 22564. (f) Kouzine, F.; Gupta, A.; Baranello, L.; Wojtowicz, D.; Ben-Aissa, K.; Liu, J.; Przytycka, T. M.; Levens, D. *Nat. Struct. Mol. Biol.* **2013**, *20*, 396.

(12) Yoshida, M.; Muneyuki, E.; Hisabori, T. *Nat. Rev. Mol. Cell Biol.* **2001**, *2*, 669.

(13) Watanabe, R.; Noji, H. *FEBS Lett.* **2013**, *587*, 1030.

(14) Imada, K.; Minamino, T.; Tahara, A.; Namba, K. *Proc. Natl. Acad. Sci. U.S.A.* **2007**, *104*, 485.

(15) Kishikawa, J.-i.; Ibuki, T.; Nakamura, S.; Nakanishi, A.; Minamino, T.; Miyata, T.; Namba, K.; Konno, H.; Ueno, H.; Imada, K. *PLoS One* **2013**, *8*, e64695.

(16) (a) Liu, R.; Ochman, H. *J. Bacteriol.* **2007**, *189*, 7098. (b) Snyder, L. A.; Loman, N. J.; Fütterer, K.; Pallen, M. J. *Trends Microbiol.* **2009**, *17*, 1.

(17) Wang, M. D.; Schnitzer, M. J.; Yin, H.; Landick, R.; Gelles, J.; Block, S. M. *Science* **1998**, *282*, 902.

(18) Harada, Y.; Ohara, O.; Takatsuki, A.; Itoh, H.; Shimamoto, N.; Kinosita, K., Jr. *Nature* **2001**, *409*, 113.

(19) Osheroff, N.; Bjornsti, M.-A. *DNA topoisomerase protocols*; Humana Press: Totowa, N.J., 1999.

(20) Hugel, T.; Michaelis, J.; Hetherington, C. L.; Jardine, P. J.; Grimes, S.; Walter, J. M.; Falk, W.; Anderson, D. L.; Bustamante, C. *PLoS Biology* **2007**, *5*, e59.

(21) Vinograd, J.; Lebowitz, J.; Radloff, R.; Watson, R.; Laipis, P. *Proc. Natl. Acad. Sci. U.S.A.* **1965**, *53*, 1104.

(22) Drew, H. R.; Samson, S.; Dickerson, R. E. *Proc. Natl. Acad. Sci. U.S.A.* **1982**, *79*, 4040.

(23) (a) Silverman, M.; Simon, M. *Nature* **1974**, *249*, 73. (b) Berg, H. C. *Nature* **1974**, *249*, 77. (c) Block, S. M.; Segall, J. E.; Berg, H. C. *J. Bacteriol.* **1983**, *154*, 312.

(24) (a) Turner, L.; Ryu, W. S.; Berg, H. C. *J. Bacteriol.* **2000**, *182*, 2793. (b) Darnton, N. C.; Turner, L.; Rojevsky, S.; Berg, H. C. *J. Bacteriol.* **2007**, *189*, 1756.

(25) (a) Ryu, W. S.; Berry, R. M.; Berg, H. C. *Nature* **2000**, *403*, 444. (b) Chen, X.; Berg, H. C. *Biophys. J.* **2000**, *78*, 1036. (c) Sowa, Y.; Rowe, A. D.; Leake, M. C.; Yakushi, T.; Homma, M.; Ishijima, A.; Berry, R. M. *Nature* **2005**, *437*, 916. (d) Reid, S. W.; Leake, M. C.; Chandler, J. H.; Lo, C. J.; Armitage, J. P.; Berry, R. M. *Proc. Natl. Acad. Sci. U.S.A.* **2006**, *103*, 8066.

(26) (a) Sowa, Y.; Hotta, H.; Homma, M.; Ishijima, A. *J. Mol. Biol.* **2003**, *327*, 1043. (b) Inoue, Y.; Lo, C. J.; Fukuoka, H.; Takahashi, H.; Sowa, Y.; Pilizota, T.; Wadhams, G. H.; Homma, M.; Berry, R. M.; Ishijima, A. *J. Mol. Biol.* **2008**, *376*, 1251. (c) Lo, C. J.; Sowa, Y.; Pilizota, T.; Berry, R. M. *Proc. Natl. Acad. Sci. U.S.A.* **2013**, *110*, E2544.

(27) Yasuda, R.; Miyata, H.; Kinosita, K., Jr. *J. Mol. Biol.* **1996**, *263*, 227.

(28) (a) Bryant, Z.; Stone, M. D.; Gore, J.; Smith, S. B.; Cozzarelli, N. R.; Bustamante, C. *Nature* **2003**, *424*, 338. (b) Lipfert, J.; Wiggin, M.; Kerssemakers, J. W.; Pedaci, F.; Dekker, N. H. *Nat. Commun.* **2011**, *2*, 439.

(29) Noji, H.; Yasuda, R.; Yoshida, M.; Kinosita, K., Jr. *Nature* **1997**, *386*, 299.

(30) Yasuda, R.; Noji, H.; Yoshida, M.; Kinosita, K., Jr.; Itoh, H. *Nature* **2001**, *410*, 898.

(31) Hayashi, M.; Harada, Y. *Nucleic Acids Res.* **2007**, *35*, e125.

(32) Vale, R. D.; Yano Toyoshima, Y. *Cell* **1988**, *52*, 459.

(33) Walker, R. A.; Salmon, E. D.; Endow, S. A. *Nature* **1990,** *347*, 780.

(34) Gutiérrez-Medina, B.; Fehr, A. N.; Block, S. M. *Proc. Natl. Acad. Sci. U.S.A.* **2009**, *106*, 17007.

(35) Brunnbauer, M.; Dombi, R.; Ho, T. H.; Schliwa, M.; Rief, M.; Okten, Z. *Mol. Cell* **2012**, *46*, 147.
(36) (a) Foster, K. R.; Sauer, F. A.; Schwan, H. P. *Biophys. J.* **1992**, *63*, 180. (b) Jones, T. B. *Engineering in Medicine and Biology Magazine, IEEE* **2003**, *22*, 33.
(37) Washizu, M.; Kurahashi, Y.; Iochi, H.; Kurosawa, O.; Aizawa, S.; Kudo, S.; Magariyama, Y.; Hotani, H. *IEEE Transactions on Industry Applications* **1993**, *29*, 286.
(38) (a) Berg, H. C.; Turner, L. *Biophys. J.* **1993**, *65*, 2201. (b) Berry, R. M.; Turner, L.; Berg, H. C. *Biophys. J.* **1995**, *69*, 280. (c) Berg, H. C. *Annu. Rev. Biochem.* **2003**, *72*, 19. (d) Sowa, Y.; Berry, R. M. *Q. Rev. Biophys.* **2008**, *41*, 103.
(39) (a) Watanabe-Nakayama, T.; Toyabe, S.; Kudo, S.; Sugiyama, S.; Yoshida, M.; Muneyuki, E. *Biochem. Biophys. Res. Commun.* **2008**, *366*, 951. (b) Toyabe, S.; Okamoto, T.; Watanabe-Nakayama, T.; Taketani, H.; Kudo, S.; Muneyuki, E. *Phys. Rev. Lett.* **2010**, *104*, 198103. (c) Toyabe, S.; Watanabe-Nakayama, T.; Okamoto, T.; Kudo, S.; Muneyuki, E. *Proc. Natl. Acad. Sci. U.S.A.* **2011**, *108*, 17951.
(40) Berry, R. M.; Berg, H. C. *Biophys. J.* **1996**, *71*, 3501.
(41) Lipfert, J.; Hao, X.; Dekker, N. H. *Biophys. J.* **2009**, *96*, 5040.
(42) (a) Ribeck, N.; Saleh, O. A. *Rev. Sci. Instrum.* **2008**, *79*, 094301. (b) De Vlaminck, I.; Henighan, T.; van Loenhout, M. T.; Pfeiffer, I.; Huijts, J.; Kerssemakers, J. W.; Katan, A. J.; van Langen-Suurling, A.; van der Drift, E.; Wyman, C.; Dekker, C. *Nano Lett.* **2011**, *11*, 5489.
(43) Neuman, K. C.; Chadd, E. H.; Liou, G. F.; Bergman, K.; Block, S. M. *Biophys. J.* **1999**, *77*, 2856.
(44) Dulin, D.; Lipfert, J.; Moolman, M. C.; Dekker, N. H. *Nat. Rev. Genet.* **2012**, *14*, 9.
(45) (a) Strick, T. R.; Allemand, J. F.; Bensimon, D.; Bensimon, A.; Croquette, V. *Science* **1996**, *271*, 1835. (b) Lipfert, J.; Koster, D. A.; Vilfan, I. D.; Hage, S.; Dekker, N. H. *Methods in molecular biology* **2009**, *582*, 71. (c) Vilfan, I. D.; Lipfert, J.; Koster, D. A.; Lemay, S. G.; Dekker, N. H. In *Handbook of Single-Molecule Biophysics*; Hinterdorfer, P., van Oijen, A., Eds.; Springer: Heidelberg, 2009. (d) Dulin, D.; Lipfert, J.; Moolman, M. C.; Dekker, N. H. *Nat. Rev. Genet.* **2013**, *14*, 9.
(46) (a) Gosse, C.; Croquette, V. *Biophys. J.* **2002**, *82*, 3314. (b) Mosconi, F.; Allemand, J. F.; Croquette, V. *Rev. Sci. Instrum.* **2011**, *82*, 12.
(47) Strick, T. R.; Allemand, J. F.; Bensimon, D.; Croquette, V. *Biophys. J.* **1998**, *74*, 2016.
(48) Lipfert, J.; Skinner, G. M.; Keegstra, J. M.; Hensgens, T.; Jager, T.; Dulin, D.; Kober, M.; Yu, Z.; Donkers, S. P.; Chou, F. C.; Das, R.; Dekker, N. H. *Proc. Natl. Acad. Sci. U.S.A.* **2014**.
(49) Strick, T. R.; Croquette, V.; Bensimon, D. *Nature* **2000**, *404*, 901.
(50) Dekker, N. H.; Rybenkov, V. V.; Duguet, M.; Crisona, N. J.; Cozzarelli, N. R.; Bensimon, D.; Croquette, V. *Proc. Natl. Acad. Sci. U.S.A.* **2002**, *99*, 12126.
(51) (a) Koster, D. A.; Croquette, V.; Dekker, C.; Shuman, S.; Dekker, N. H. *Nature* **2005**, *434*, 671. (b) Koster, D. A.; Palle, K.; Bot, E. S.; Bjornsti, M. A.; Dekker, N. H. *Nature* **2007**, *448*, 213.
(52) Taneja, B.; Schnurr, B.; Slesarev, A.; Marko, J. F.; Mondragon, A. *Proc. Natl. Acad. Sci. U.S.A.* **2007**, *104*, 14670.
(53) Revyakin, A.; Liu, C.; Ebright, R. H.; Strick, T. R. *Science* **2006**, *314*, 1139.
(54) Crut, A.; Nair, P. A.; Koster, D. A.; Shuman, S.; Dekker, N. H. *Proc. Natl. Acad. Sci. U.S.A.* **2008**, *105*, 6894.
(55) Bai, H.; Sun, M.; Ghosh, P.; Hatfull, G. F.; Grindley, N. D.; Marko, J. F. *Proc. Natl. Acad. Sci. U.S.A.* **2011**, *108*, 7419.
(56) (a) Strick, T. R.; Dessinges, M. N.; Charvin, G.; Dekker, N. H.; Allemand, J. F.; Bensimon, D.; Croquette, V. *Reports on Progress in Physics* **2003**, *66*, 1. (b) Mosconi, F.; Allemand, J. F.; Bensimon, D.; Croquette, V. *Phys. Rev. Lett.* **2009**, *102*, 078301. (c) Marko, J. F. *Phys. Rev. E Stat Nonlin Soft Matter Phys* **2007**, *76*, 021926.
(57) (a) De Vlaminck, I.; Vidic, I.; van Loenhout, M. T.; Kanaar, R.; Lebbink, J. H.; Dekker, C. *Nucleic Acids Res.* **2010,** *38,* 4133 . (b) Maffeo, C.; Schopflin, R.; Brutzer, H.; Stehr, R.; Aksimentiev, A.; Wedemann, G.; Seidel, R. *Phys. Rev. Lett.* **2010**, *105*, 158101.
(58) (a) Marko, J. F.; Neukirch, S. *Phys. Rev. E Stat Nonlin Soft Matter Phys* **2012**, *85*, 011908. (b) Schopflin, R.; Brutzer, H.; Muller, O.; Seidel, R.; Wedemann, G. *Biophys. J.* **2012**, *103*, 323. (c) Emanuel, M.; Lanzani, G.; Schiessel, H. *Phys. Rev. E Stat Nonlin Soft Matter Phys* **2013**, *88*, 022706.
(59) (a) Celedon, A.; Wirtz, D.; Sun, S. *J. Phys. Chem. B* **2010**, *114*, 16929. (b) Lipfert, J.; Klijnhout, S.; Dekker, N. H. *Nucleic Acids Res.* **2010**, *38*, 7122. (c) Lipfert, J.; Kerssemakers, J. W.; Jager, T.; Dekker, N. H. *Nat. Methods* **2010**, *7*, 977. (d) Lee, M.; Lipfert, J.; Sanchez, H.; Wyman, C.; Dekker, N. H. *Nucleic Acids Res.* **2013**, *41*, 7023.
(60) (a) Celedon, A.; Nodelman, I. M.; Wildt, B.; Dewan, R.; Searson, P.; Wirtz, D.; Bowman, G. D.; Sun, S. X. *Nano Lett.* **2009**, *9*, 1720. (b) Lipfert, J.; Kerssemakers, J. J.; Rojer, M.; Dekker, N. H. *The Rev. Sci. Instrum.* **2011**, *82*, 103707.
(61) Han, Y. W.; Tani, T.; Hayashi, M.; Hishida, T.; Iwasaki, H.; Shinagawa, H.; Harada, Y. *Proc. Natl. Acad. Sci. U.S.A.* **2006**, *103*, 11544.

(62) Arata, H.; Dupont, A.; Mine-Hattab, J.; Disseau, L.; Renodon-Corniere, A.; Takahashi, M.; Viovy, J. L.; Cappello, G. *Proc. Natl. Acad. Sci. U.S.A.* **2009**, *106*, 19239.
(63) Gore, J.; Bryant, Z.; Nollmann, M.; Le, M. U.; Cozzarelli, N. R.; Bustamante, C. *Nature* **2006**, *442*, 836.
(64) (a) Oberstrass, F. C.; Fernandes, L. E.; Lebel, P.; Bryant, Z. *Phys. Rev. Lett.* **2013**, *110*, 178103. (b) Oberstrass, F. C.; Fernandes, L. E.; Bryant, Z. *Proc. Natl. Acad. Sci. U.S.A.* **2012**, *109*, 6106.
(65) (a) Gore, J.; Bryant, Z.; Stone, M. D.; Nollmann, M.; Cozzarelli, N. R.; Bustamante, C. *Nature* **2006**, *439*, 100. (b) Basu, A.; Schoeffler, A. J.; Berger, J. M.; Bryant, Z. *Nat. Struct. Mol. Biol.* **2012**, *19*, 538.
(66) Lebel, P.; Basu, A.; Oberstrass, F. C.; Tretter, E. M.; Bryant, Z. *Nat. Methods* **2014**, *11*, 456.
(67) Kauert, D. J.; Kurth, T.; Liedl, T.; Seidel, R. *Nano Lett.* **2011**, *11*, 5558.
(68) Janssen, X. J.; Lipfert, J.; Jager, T.; Daudey, R.; Beekman, J.; Dekker, N. H. *Nano Lett.* **2012**, *12*, 3634.
(69) Ashkin, A.; Dziedzic, J. M.; Bjorkholm, J. E.; Chu, S. *Opt. Lett.* **1986**, *11*, 288.
(70) (a) Capitanio, M.; Pavone, F. S. *Biophys. J.* **2013**, *105*, 1293. (b) Neuman, K. C.; Block, S. M. *Rev. Sci. Instrum.* **2004**, *75*, 2787. (c) Moffitt, J. R.; Chemla, Y. R.; Smith, S. B.; Bustamante, C. *Annu. Rev. Biochem.* **2008**, *77*, 205. (d) Fazal, F. M.; Block, S. M. *Nature Photon.* **2011**, *5*, 318. (e) Svoboda, K.; Block, S. M. *Annu. Rev. Biophys. Biomol. Struct.* **1994**, *23*, 247. (f) Grier, D. G. *Nature* **2003**, *424*, 810. (g) Greenleaf, W. J.; Woodside, M. T.; Block, S. M. *Annu. Rev. Biophys. Biomol. Struct.* **2007**, *36*, 171. (h) Dholakia, K.; Reece, P.; Gu, M. *Chem. Soc. Rev.* **2008**, *37*, 42. (i) Woodside, M. T.; Valentine, M. T. In *Handbook of Single-Molecule Biophysics*; Springer: Heidelberg, 2009. (j) Stevenson, D. J.; Gunn-Moore, F.; Dholakia, K. *J. Biomed. Opt.* **2010**, *15*, 041503.
(71) (a) Berry, R. M.; Berg, H. C. *Proc. Natl. Acad. Sci. U.S.A.* **1997**, *94*, 14433. (b) Block, S. M.; Blair, D. F.; Berg, H. C. *Nature* **1989**, *338*, 514. (c) Block, S. M.; Blair, D. F.; Berg, H. C. *Cytometry* **1991**, *12*, 492.
(72) Pilizota, T.; Bilyard, T.; Bai, F.; Futai, M.; Hosokawa, H.; Berry, R. M. *Biophys. J.* **2007**, *93*, 264.
(73) Bingelyte, V.; Leach, J.; Courtial, J.; Padgett, M. J. *Appl. Phys. Lett.* **2003**, *82*, 829.
(74) Asavei, T.; Nieminen, T. A.; Loke, V. L. Y.; Stilgoe, A. B.; Bowman, R.; Preece, D.; Padgett, M. J.; Heckenberg, N. R.; Rubinsztein-Dunlop, H. *New J. Phys.* **2013**, *15,* 063016.
(75) (a) Padgett, M.; Courtial, J.; Allen, L. *Phys Today* **2004**, *57*, 35. (b) Padgett, M.; Allen, L. *Contemp Phys* **2000**, *41*, 275. (c) Padgett, M.; Bowman, R. *Nature Photon.* **2011**, *5*, 343. (d) Yao, A. M.; Padgett, M. J. *Adv. Opt. Photon.* **2011**, *3*, 161.
(76) (a) Curtis, J. E.; Grier, D. G. *Phys. Rev. Lett.* **2003**, *90*, 133901. (b) Curtis, J. E.; Grier, D. G. *Opt. Lett.* **2003**, *28*, 872.
(77) O'Neil, A. T.; MacVicar, I.; Allen, L.; Padgett, M. J. *Phys. Rev. Lett.* **2002**, *88,* 053601.
(78) Asavei, T.; Loke, V. L. Y.; Barbieri, M.; Nieminen, T. A.; Heckenberg, N. R.; Rubinsztein-Dunlop, H. *New J. Phys.* **2009**, *11,* 093021.
(79) Allen, L.; Beijersbergen, M. W.; Spreeuw, R. J.; Woerdman, J. P. *Phys. Rev. A At. Mol. Opt. Phys.* **1992**, *45*, 8185.
(80) He, H.; Friese, M. E.; Heckenberg, N. R.; Rubinsztein-Dunlop, H. *Phys. Rev. Lett.* **1995**, *75*, 826.
(81) Beth, R. A. *Phys. Rev.* **1936**, *50*, 115.
(82) Friese, M. E. J.; Nieminen, T. A.; Heckenberg, N. R.; Rubinsztein-Dunlop, H. *Nature* **1998**, *394*, 348.
(83) La Porta, A.; Wang, M. D. *Phys. Rev. Lett.* **2004**, *92*, 190801.
(84) Oroszi, L.; Galajda, P.; Kirei, H.; Bottka, S.; Ormos, P. *Phys. Rev. Lett.* **2006**, *97*, 058301.
(85) (a) Bryant, H. C.; Sergatskov, D. A.; Lovato, D.; Adolphi, N. L.; Larson, R. S.; Flynn, E. R. *Phys. Med. Biol.* **2007**, *52*, 4009. (b) Neuman, K. C.; Lionnet, T.; Allemand, J. F. *Annu. Rev. Mater. Res.* **2007**, *37*, 33.
(86) (a) te Velthuis, A.; Kerssemakers, J. W. J.; Lipfert, J.; Dekker, N. H. *Biophys. J.* **2010**, *99*, 1292. (b) Wong, W. P.; Halvorsen, K. *Opt. Express* **2006**, *14*, 12517. (c) Wong, W. P.; Halvorsen, K. *Opt. Lett.* **2009**, *34*, 277. (d) Otto, O.; Czerwinski, F.; Gornall, J. L.; Stober, G.; Oddershede, L. B.; Seidel, R.; Keyser, U. F. *Opt. Express* **2010**, *18*, 22722. (e) Lansdorp, B. M.; Saleh, O. A. *The Rev. Sci. Instrum.* **2012**, *83*, 025115.
(87) Normanno, D.; Capitanio, M.; Pavone, F. S. *Phys. Rev. A At. Mol. Opt. Phys.* **2004**, *70*, 8.
(88) Klaue, D.; Seidel, R. *Phys. Rev. Lett.* **2009**, *102*, 028302.
(89) van Reenen, A.; Gutierrez-Mejia, F.; van, I. L. J.; Prins, M. W. *Biophys. J.* **2013**, *104*, 1073.
(90) Janssen, X. J.; Schellekens, A. J.; van Ommering, K.; van Ijzendoorn, L. J.; Prins, M. W. *Biosens. Bioelectron.* **2008**, *23,* 833.
(91) (a) Faxen, H. *Ann. Phys. (Berlin)* **1922**, *68*, 89. (b) Leach, J.; Mushfique, H.; Keen, S.; Di Leonardo, R.; Ruocco, G.; Cooper, J. M.; Padgett, M. J. *Phys. Rev. E Stat Nonlin Soft Matter Phys* **2009**, *79*, 026301.
(92) Friese, M. E. J.; Enger, J.; Rubinsztein-Dunlop, H.; Heckenberg, N. R. *Phys. Rev. A At. Mol. Opt. Phys.* **1996**, *54*, 1593.
(93) Simpson, N. B.; Dholakia, K.; Allen, L.; Padgett, M. J. *Opt. Lett.* **1997**, *22*, 52.
(94) (a) Ruijgrok, P. V.; Verhart, N. R.; Zijlstra, P.; Tchebotareva, A. L.; Orrit, M. *Phys. Rev. Lett.* **2011**, *107*. (b) Wang, K.; Schonbrun, E.; Steinvurzel, P.; Crozier, K. B. *Nat. Commun.* **2011**, *2*.

(95) Volke-Sepulveda, K.; Garces-Chavez, V.; Chavez-Cerda, S.; Arlt, J.; Dholakia, K. *J.Opt. B Quantum Semiclassical Opt.* **2002**, *4*, S82.
(96) (a) Galajda, P.; Ormos, P. *Appl. Phys. Lett.* **2001**, *78*, 249. (b) Galajda, P.; Ormos, P. *Appl. Phys. Lett.* **2002**, *80*, 4653. (c) Galajda, P.; Ormos, P. *J.Opt. B Quantum Semiclassical Opt.* **2002**, *4*, S78.
(97) Maruo, S.; Nakamura, O.; Kawata, S. *Opt. Lett.* **1997**, *22*, 132.
(98) Friese, M. E. J.; Rubinsztein-Dunlop, H.; Gold, J.; Hagberg, P.; Hanstorp, D. *Appl. Phys. Lett.* **2001**, *78*, 547.
(99) (a) Bishop, A. I.; Nieminen, T. A.; Heckenberg, N. R.; Rubinsztein-Dunlop, H. *Phys. Rev. A At. Mol. Opt. Phys.* **2003**, *68*. (b) Gutierrez-Medina, B.; Andreasson, J. O.; Greenleaf, W. J.; Laporta, A.; Block, S. M. *Meth. Enzymol.* **2010**, *475*, 377.
(100) Hecht, E.; Zając, A. *Optics*; 2nd ed.; Addison-Wesley Pub. Co.: Reading, Mass., 1987.
(101) Visscher, K.; Block, S. M. *Meth. Enzymol.* **1998**, *298*, 460.
(102) Sasaki, K.; Koshioka, M.; Misawa, H.; Kitamura, N.; Masuhara, H. *Jpn. J. Appl. Phys.* **1991**, *30*, L907.
(103) Curtis, J. E.; Koss, B. A.; Grier, D. G. *Opt. Commun.* **2002**, *207*, 169.
(104) Jackson, J. D. *Classical Electrodynamics - Third edition*; Wiley: Hoboken, 1999.
(105) (a) Nieminen, T. A.; Heckenberg, N. R.; Rubinsztein-Dunlop, H. *J. Mod. Opt.* **2001**, *48*, 405. (b) Wulff, K. D.; Cole, D. G.; Clark, R. L. *Appl. Optics* **2008**, *47*, 6428.
(106) (a) Shelton, W. A.; Bonin, K. D.; Walker, T. G. *Phys. Rev. E Stat Nonlin Soft Matter Phys* **2005**, *71*, 036204. (b) Ji, N.; Liu, M.; Zhou, J.; Lin, Z.; Chui, S. *Opt. Express* **2005**, *13*, 5192.
(107) (a) Liu, M. K.; Ji, N.; Lin, Z. F.; Chui, S. T. *Phys. Rev. E Stat Nonlin Soft Matter Phys* **2005**, *72*. (b) Simpson, S. H.; Benito, D. C.; Hanna, S. *Phys. Rev. A At. Mol. Opt. Phys.* **2007**, *76*. (c) Simpson, S. H.; Hanna, S. *Opt. Express* **2011**, *19*, 16526.
(108) Ghosh, G. *Opt. Commun.* **1999**, *163*, 95.
(109) (a) Bishop, A. I.; Nieminen, T. A.; Heckenberg, N. R.; Rubinsztein-Dunlop, H. *Phys. Rev. Lett.* **2004**, *92*, 198104. (b) Vogel, R.; Persson, M.; Feng, C.; Parkin, S. J.; Nieminen, T. A.; Wood, B.; Heckenberg, N. R.; Rubinsztein-Dunlop, H. *Langmuir* **2009**, *25*, 11672.
(110) (a) Deufel, C.; Forth, S.; Simmons, C. R.; Dejgosha, S.; Wang, M. D. *Nat. Methods* **2007**, *4*, 223. (b) Huang, Z.; Pedaci, F.; van Oene, M.; Wiggin, M. J.; Dekker, N. H. *ACS nano* **2011**, *5*, 1418. (c) Li, P.-C.; Chang, J.-C.; Porta, A. L.; Yu, E. T. *Nanotechnology* **2014**, *25*, 235304.
(111) Singer, W.; Nieminen, T. A.; Gibson, U. J.; Heckenberg, N. R.; Rubinsztein-Dunlop, H. *Phys. Rev. E Stat Nonlin Soft Matter Phys* **2006**, *73*, 021911.
(112) Pedaci, F.; Huang, Z. X.; van Oene, M.; Barland, S.; Dekker, N. H. *Nature Physics* **2011**, *7*, 259.
(113) Pedaci, F.; Huang, Z.; van Oene, M.; Dekker, N. H. *Opt. Express* **2012**, *20*, 3787.
(114) Inman, J.; Forth, S.; Wang, M. D. *Opt. Lett.* **2010**, *35*, 2949.
(115) Parkin, S. J.; Vogel, R.; Persson, M.; Funk, M.; Loke, V. L. Y.; Nieminen, T. A.; Heckenberg, N. R.; Rubinsztein-Dunlop, H. *Opt. Express* **2009**, *17*, 21944.
(116) (a) Lansdorp, B. M.; Tabrizi, S. J.; Dittmore, A.; Saleh, O. A. *The Rev. Sci. Instrum.* **2013**, *84*, 044301. (b) Cnossen, J. P.; Dulin, D.; Dekker, N. H. *The Rev. Sci. Instrum.* **2014**, *85*, 103712.
(117) Capitanio, M.; Cicchi, R.; Saverio Pavone, F. *Opt. Laser Eng.* **2007**, *45*, 450.
(118) Bustamante, C.; Bryant, Z.; Smith, S. B. *Nature* **2003**, *421*, 423.
(119) Bryant, Z.; Oberstrass, F. C.; Basu, A. *Curr. Opin. Chem. Biol.* **2012**, *22*, 304.
(120) (a) Abels, J. A.; Moreno-Herrero, F.; van der Heijden, T.; Dekker, C.; Dekker, N. H. *Biophys. J.* **2005**, *88*, 2737. (b) Herrero-Galan, E.; Fuentes-Perez, M. E.; Carrasco, C.; Valpuesta, J. M.; Carrascosa, J. L.; Moreno-Herrero, F.; Arias-Gonzalez, J. R. *J Am Chem Soc* **2013**, *135*, 122.
(121) (a) Sheinin, M. Y.; Wang, M. D. *Phys Chem Chem Phys* **2009**, *11*, 4800. (b) Sheinin, M. Y.; Forth, S.; Marko, J. F.; Wang, M. D. *Phys. Rev. Lett.* **2011**, *107*, 108102.
(122) Forth, S.; Sheinin, M. Y.; Inman, J.; Wang, M. D. *Annual review of biophysics* **2013**, *42*, 583.
(123) Strick, T. R.; Croquette, V.; Bensimon, D. *Proc. Natl. Acad. Sci. U.S.A.* **1998**, *95*, 10579.
(124) Allemand, J. F.; Bensimon, D.; Lavery, R.; Croquette, V. *Proc. Natl. Acad. Sci. U.S.A.* **1998**, *95*, 14152.
(125) (a) Gessner, R. V.; Frederick, C. A.; Quigley, G. J.; Rich, A.; Wang, A. H. *The Journal of biological chemistry* **1989**, *264*, 7921. (b) Wang, A. H.; Quigley, G. J.; Kolpak, F. J.; Crawford, J. L.; van Boom, J. H.; van der Marel, G.; Rich, A. *Nature* **1979**, *282*, 680. (c) Pohl, F. M.; Jovin, T. M. *J. Mol. Biol.* **1972**, *67*, 375.
(126) Rich, A.; Nordheim, A.; Wang, A. H. *Annu. Rev. Biochem.* **1984**, *53*, 791.
(127) Lee, M.; Kim, S. H.; Hong, S. C. *Proc. Natl. Acad. Sci. U.S.A.* **2010**, *107*, 4985.
(128) (a) Nangreave, J.; Han, D.; Liu, Y.; Yan, H. *Curr Opin Chem Biol* **2010**, *14*, 608. (b) Shih, W. M.; Lin, C. *Curr. Opin. Chem. Biol.* **2010**, *20*, 276. (c) Rothemund, P. W. *Nature* **2006**, *440*, 297.
(129) Rothemund, P. W.; Andersen, E. S. *Nature* **2012**, *485*, 584.

(130) Andersen, E. S.; Dong, M.; Nielsen, M. M.; Jahn, K.; Subramani, R.; Mamdouh, W.; Golas, M. M.; Sander, B.; Stark, H.; Oliveira, C. L.; Pedersen, J. S.; Birkedal, V.; Besenbacher, F.; Gothelf, K. V.; Kjems, J. *Nature* **2009**, *459*, 73.
(131) Dietz, H.; Douglas, S. M.; Shih, W. M. *Science* **2009**, *325*, 725.
(132) Douglas, S. M.; Dietz, H.; Liedl, T.; Hogberg, B.; Graf, F.; Shih, W. M. *Nature* **2009**, *459*, 414.
(133) Chen, Z.; Yang, H.; Pavletich, N. P. *Nature* **2008**, *453*, 489.
(134) (a) Mine, J.; Disseau, L.; Takahashi, M.; Cappello, G.; Dutreix, M.; Viovy, J. L. *Nucleic Acids Res.* **2007**, *35*, 7171. (b) van der Heijden, T.; Seidel, R.; Modesti, M.; Kanaar, R.; Wyman, C.; Dekker, C. *Nucleic Acids Res.* **2007**, *35*, 5646.
(135) (a) Hegner, M.; Smith, S. B.; Bustamante, C. *Proc. Natl. Acad. Sci. U.S.A.* **1999**, *96*, 10109. (b) Shivashankar, G. V.; Feingold, M.; Krichevsky, O.; Libchaber, A. *Proc. Natl. Acad. Sci. U.S.A.* **1999**, *96*, 7916.
(136) Yoshida, M.; Okamoto, H.; Sone, N.; Hirata, H.; Kagawa, Y. *Proc. Natl. Acad. Sci. U.S.A.* **1977**, *74*, 936.
(137) (a) Boyer, P.; Kohlbrenner, W. In *Energy coupling in photosynthesis*; Selman, B., Selman-Reimer, S., Eds.; Elsevier: Amsterdam, 1981. (b) Oosawa, F.; Hayashi, S. *Advances in biophysics* **1986**, *22*, 151.
(138) Abrahams, J. P.; Leslie, A. G.; Lutter, R.; Walker, J. E. *Nature* **1994**, *370*, 621.
(139) (a) Duncan, T. M.; Bulygin, V. V.; Zhou, Y.; Hutcheon, M. L.; Cross, R. L. *Proc. Natl. Acad. Sci. U.S.A.* **1995**, *92*, 10964. (b) Zhou, Y.; Duncan, T. M.; Cross, R. L. *Proc. Natl. Acad. Sci. U.S.A.* **1997**, *94*, 10583. (c) Sabbert, D.; Engelbrecht, S.; Junge, W. *Nature* **1996**, *381*, 623.
(140) Itoh, H.; Takahashi, A.; Adachi, K.; Noji, H.; Yasuda, R.; Yoshida, M.; Kinosita, K. *Nature* **2004**, *427*, 465.
(141) Watanabe, R.; Okuno, D.; Sakakihara, S.; Shimabukuro, K.; Iino, R.; Yoshida, M.; Noji, H. *Nat. Chem. Biol.* **2012**, *8*, 86.
(142) Watanabe, R.; Okuno, D.; Sakakihara, S.; Shimabukuro, K.; Iino, R.; Yoshida, M.; Noji, H. *Nat. Chem. Biol.* **2012**, *8*, 86.
(143) (a) Lighthill, J. *SIAM Rev.* **1976**, *18*, 161. (b) Bardy, S. L.; Ng, S. Y.; Jarrell, K. F. *Microbiology* **2003**, *149*, 295.
(144) Ridgway, H. G.; Silverman, M.; Simon, M. I. *J. Bacteriol.* **1977**, *132*, 657.
(145) Berg, H. C.; Anderson, R. A. *Nature* **1973**, *245*, 380.
(146) Xing, J.; Bai, F.; Berry, R.; Oster, G. *Proc. Natl. Acad. Sci. U.S.A.* **2006**, *103*, 1260.
(147) Blair, D. F.; Berg, H. C. *Science* **1988**, *242*, 1678.
(148) (a) Lo, C. J.; Leake, M. C.; Pilizota, T.; Berry, R. M. *Biophys. J.* **2007**, *93*, 294. (b) Yuan, J.; Berg, H. C. *Proc. Natl. Acad. Sci. U.S.A.* **2008**, *105*, 1182.
(149) Humphrey, W.; Dalke, A.; Schulten, K. *J Mol Graph* **1996**, *14*, 33.
(150) (a) Bugreev, D. V.; Mazin, A. V. *Proc. Natl. Acad. Sci. U.S.A.* **2004**, *101*, 9988. (b) Atwell, S.; Disseau, L.; Stasiak, A. Z.; Stasiak, A.; Renodon-Corniere, A.; Takahashi, M.; Viovy, J. L.; Cappello, G. *Nucleic Acids Res.* **2012**, *40*, 11769.
(151) (a) Fulconis, R.; Bancaud, A.; Allemand, J. F.; Croquette, V.; Dutreix, M.; Viovy, J. L. *Biophys. J.* **2004**, *87*, 2552. (b) van der Heijden, T.; van Noort, J.; van Leest, H.; Kanaar, R.; Wyman, C.; Dekker, N. H.; Dekker, C. *Nucleic Acids Res.* **2005**, *33*, 2099.

{Asavei, 2009 #2562}

AUTHOR BIOGRAPHIES

Jan Lipfert obtained his Ph.D. from Stanford University in 2008, using a combination of computer simulations, bench top biochemistry, and small-angle X-ray scattering to study the structure, dynamics, and interactions of (membrane) proteins and RNAs. During his post doc in the lab of Nynke Dekker at Delft University of Technology, he developed novel magnetic tweezers instruments for single-molecule studies of torque and twist and applied them to investigate the mechanical properties of double-stranded DNA and RNA as well as their interactions with proteins relevant to the storage and repair of the genome. In 2013, he moved to the University of Munich, to start his own lab as an associate professor of experimental biophysics.

Maarten M. van Oene received his M.Sc in Nanoscience from TU Delft (Delft, The Netherlands) in 2010. His final year of his master's degree he assisted in the development and characterization of an optical torque wrench built in the Nynke H. Dekker group at TU Delft. In 2011, he joined that same group as a Ph.D student. Currently, his research efforts are devoted to studying the bacterial flagellar motor of Escherichia coli, in particular, torque-dependence in the performance of this flagellar motor.

Mina Lee received her Ph.D. in physical chemistry from Seoul National University. After graduation, she moved to Korea University, switching her research theme to single molecule biophysics. She developed the combined technique of FRET and magnetic tweezers and applied it to probe DNA conformational dynamics. In 2009, she moved to Max Planck Institute to work on the application of superresolution microscopy. In 2011, she joined Nynke Dekker's group at TU Delft working on the application of recently developed magnetic torque and twist tweezers assays.

Francesco Pedaci has a background of experimental physicist, specialized in optical systems. He obtained his PhD in Physics at the Institut Non Linéaire de Nice (Nice, France) working on laser non-linear effects. He worked in the development of soft-X ray laser sources in a first postdoctoral period at the Colorado

State University (Fort Collins, Colorado). His second postdoctoral research at the Bionanoscience department at TU Delft (Delft, The Netherlands) was devoted to single-molecule biophysics employing optical systems. In 2012 he started his group at the Centre de Biochimie Structurale (Montpellier, France) as a CNRS researcher.

Nynke H. Dekker obtained her PhD in physics at Harvard University (Cambridge, USA) in 2000. She performed her postdoctoral work in biophysics at the Ecole Normale Supérieure (Paris, France). Since 2002, she has headed her single-molecule biophysics group at TU Delft. Her group has contributed to the understanding of mechanism of topoisomerases, quantitatively examined drug inhibition of enzymatic function at the single-molecule level, and examined the structural properties of both DNA and RNA. Most recently, her group has developed novel magnetic tweezers instruments for the measurement of twist and torque. Nynke Dekker has been a member of the Council of the Biophysical Society and organized several conferences in the area of single-molecule biophysics.

Table 1. Friction coefficients and time scales of rotational motion for beads of different sizes.

Bead radius (μm)	Friction coefficient γ_θ for rotation about an axis through the equator*) (pN·nm·s)	Time scale for rotational motion for free rotation of a 1 kbp DNA segment**) (s)
0.1	0.04	0.04
0.25	0.7	0.6
0.5	5.5	4.6
1.4	120	100

*)Computed using Equation 13, with $R_{bead} = R_{circle}$.

**)Computed as $\tau_C = \gamma_\theta / k_\theta$ with k_θ given by Equation 2, assuming C = 100 nm.

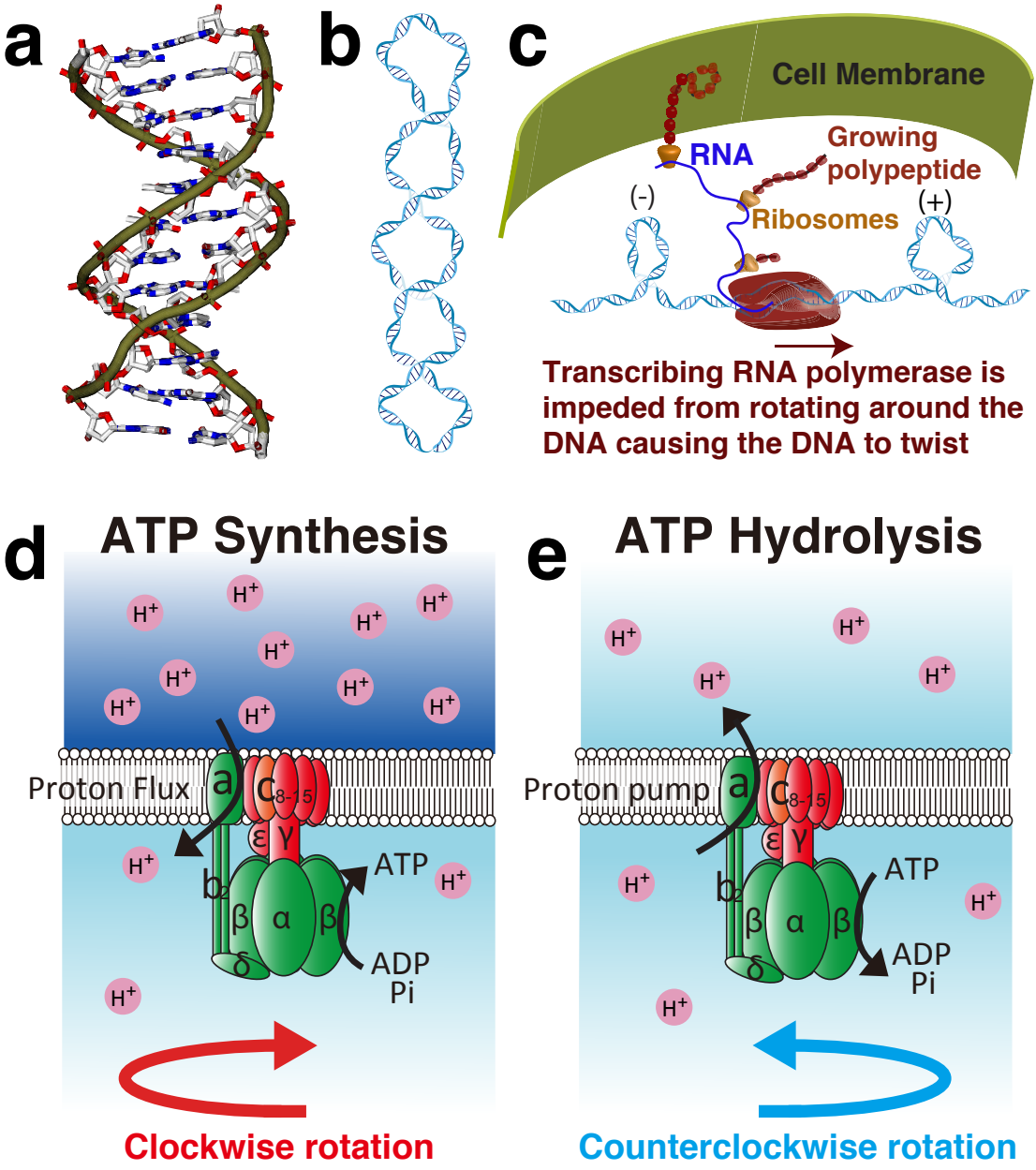
a
b
c
Cell Membrane
RNA
Growing polypeptide
(-)
Ribosomes
(+)
Transcribing RNA polymerase is impeded from rotating around the DNA causing the DNA to twist
d
ATP Synthesis
Proton Flux
a
c8-15
ε
γ
b2
β
α
β
δ
ATP
ADP
Pi
H+
Clockwise rotation
e
ATP Hydrolysis
Proton pump
Counterclockwise rotation

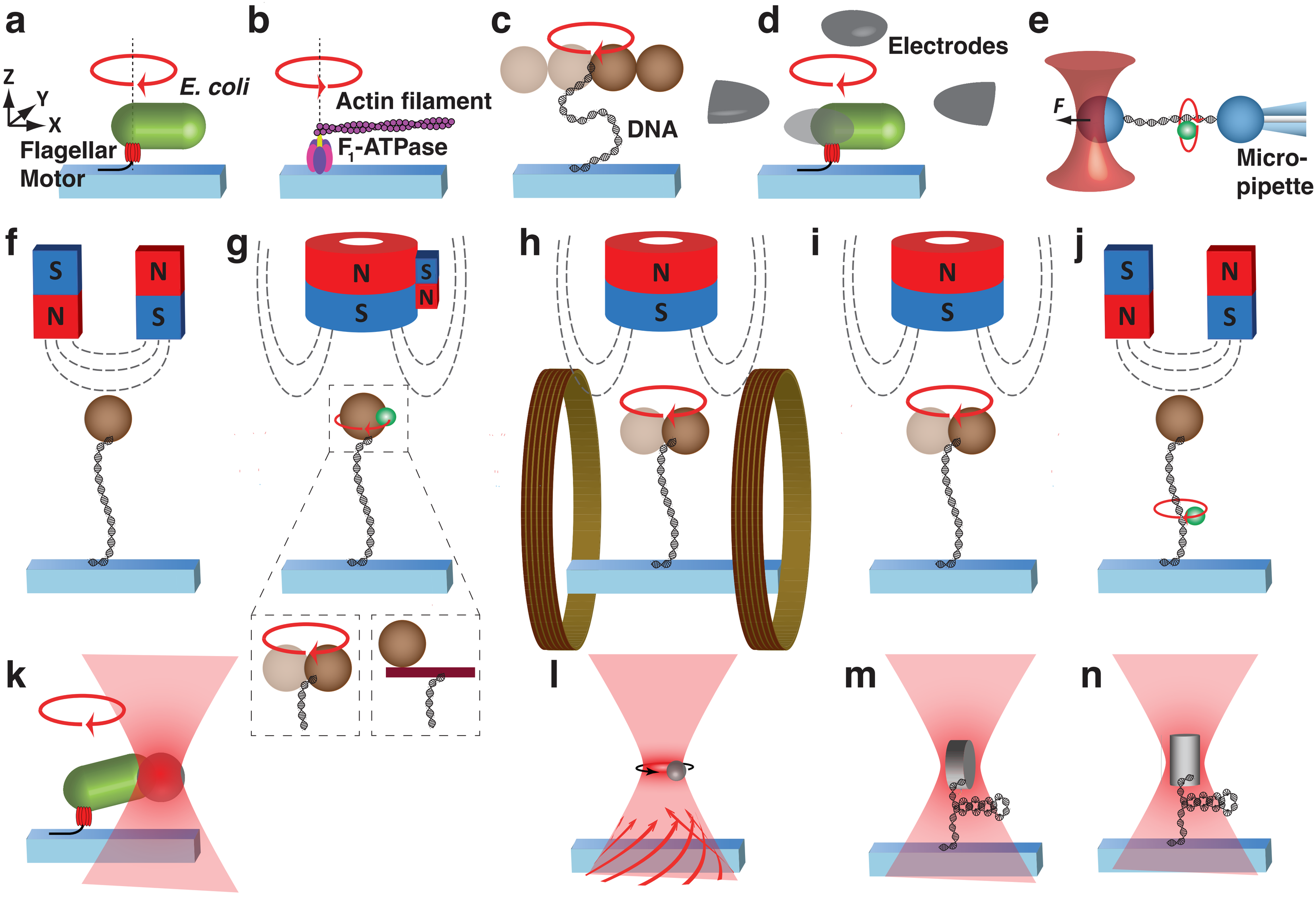
a
Z
Y
X
E. coli
Flagellar
Motor
b
Actin filament
F1-ATPase
c
DNA
d
Electrodes
e
F
Micro-
pipette
f
S
N
N
S
g
N
S
S
N
h
N
S
i
N
S
j
S
N
N
S
k
l
m
n

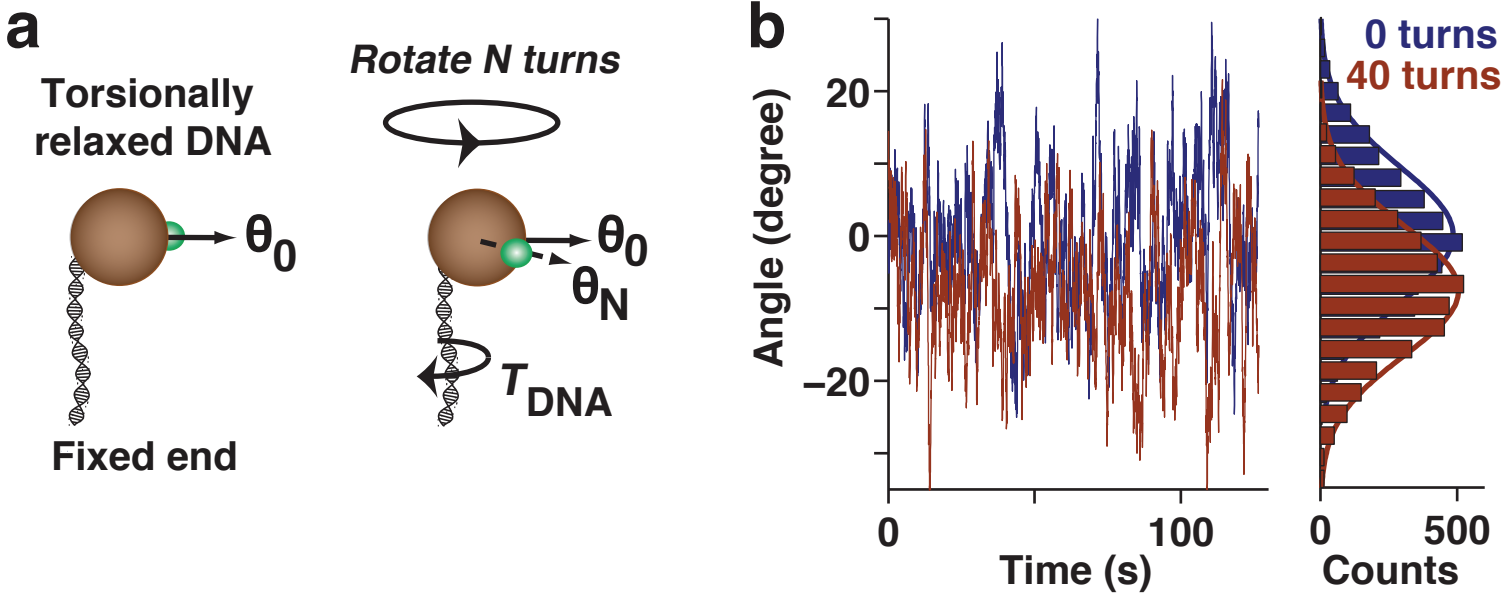
a
Torsionally relaxed DNA
θ0
Fixed end
Rotate N turns
θ0
θN
T DNA
b
Angle (degree)
20
0
–20
0
100
Time (s)
0 turns
40 turns
0
500
Counts

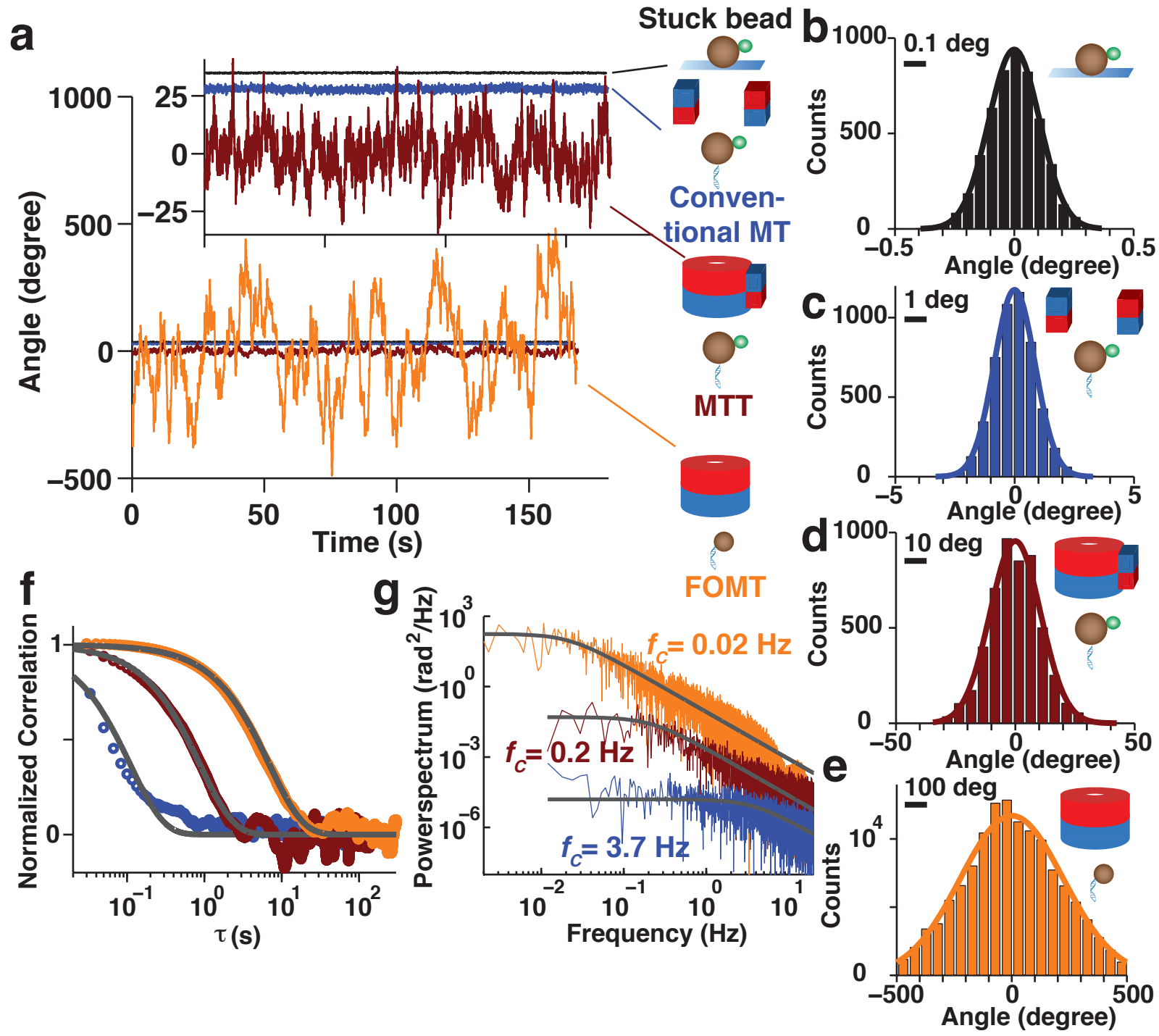
a
Stuck bead
Conven-
tional MT
MTT
FOMT
Angle (degree)
Time (s)
b
0.1 deg
Counts
Angle (degree)
c
1 deg
Counts
Angle (degree)
d
10 deg
Counts
Angle (degree)
e
100 deg
Counts
Angle (degree)
f
Normalized Correlation
τ (s)
g
Powerspectrum (rad²/Hz)
f_c= 0.02 Hz
f_c= 0.2 Hz
f_c= 3.7 Hz
Frequency (Hz)

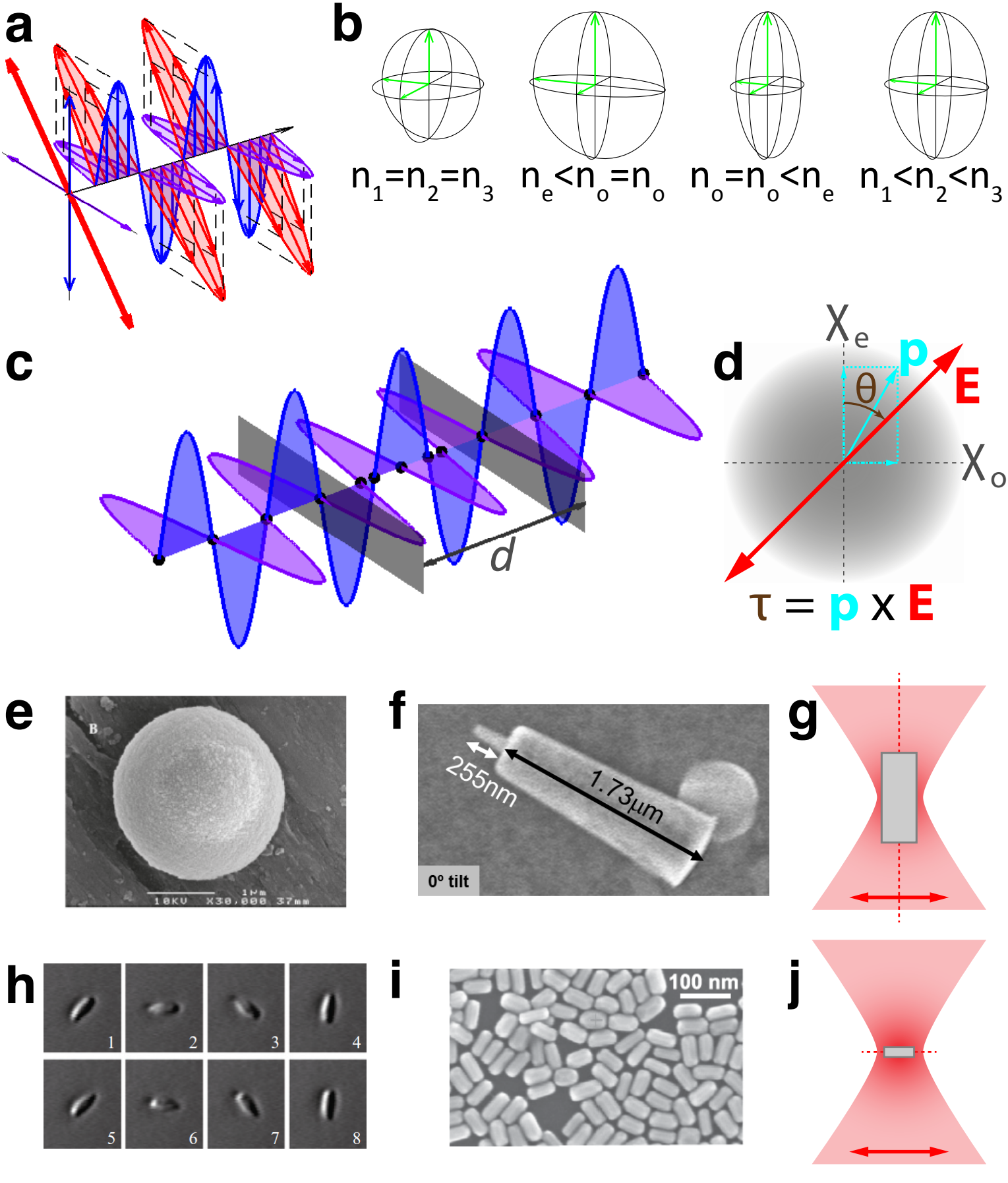
a
b
$n_1=n_2=n_3$
$n_e<n_o=n_o$
$n_o=n_o<n_e$
$n_1<n_2<n_3$
c
d
X_e
p
E
θ
X_o
τ = p x E
e
B
1KV X30,000 37mm
f
255nm
1.73μm
0° tilt
g
h
1
2
3
4
5
6
7
8
i
100 nm
j

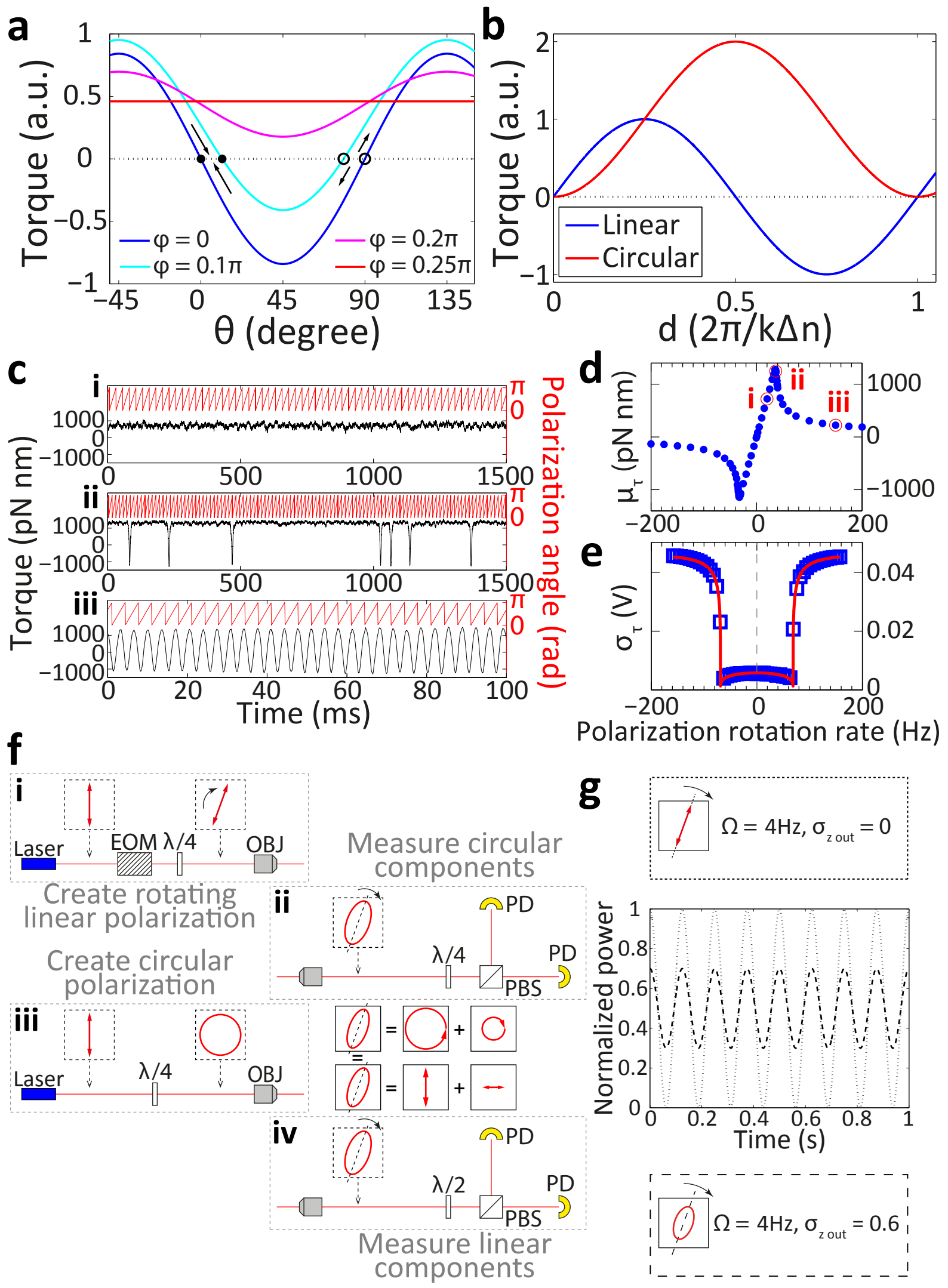
a
Torque (a.u.)
θ (degree)
φ = 0
φ = 0.1π
φ = 0.2π
φ = 0.25π
b
Torque (a.u.)
d (2π/kΔn)
Linear
Circular
c
Torque (pN nm)
Time (ms)
Polarization angle (rad)
i
ii
iii
d
μτ (pN nm)
e
στ (V)
Polarization rotation rate (Hz)
f
Laser
EOM λ/4
OBJ
Create rotating linear polarization
Create circular polarization
Measure circular components
PD
λ/4
PBS
λ/2
Measure linear components
g
Ω = 4Hz, σz out = 0
Ω = 4Hz, σz out = 0.6
Normalized power
Time (s)

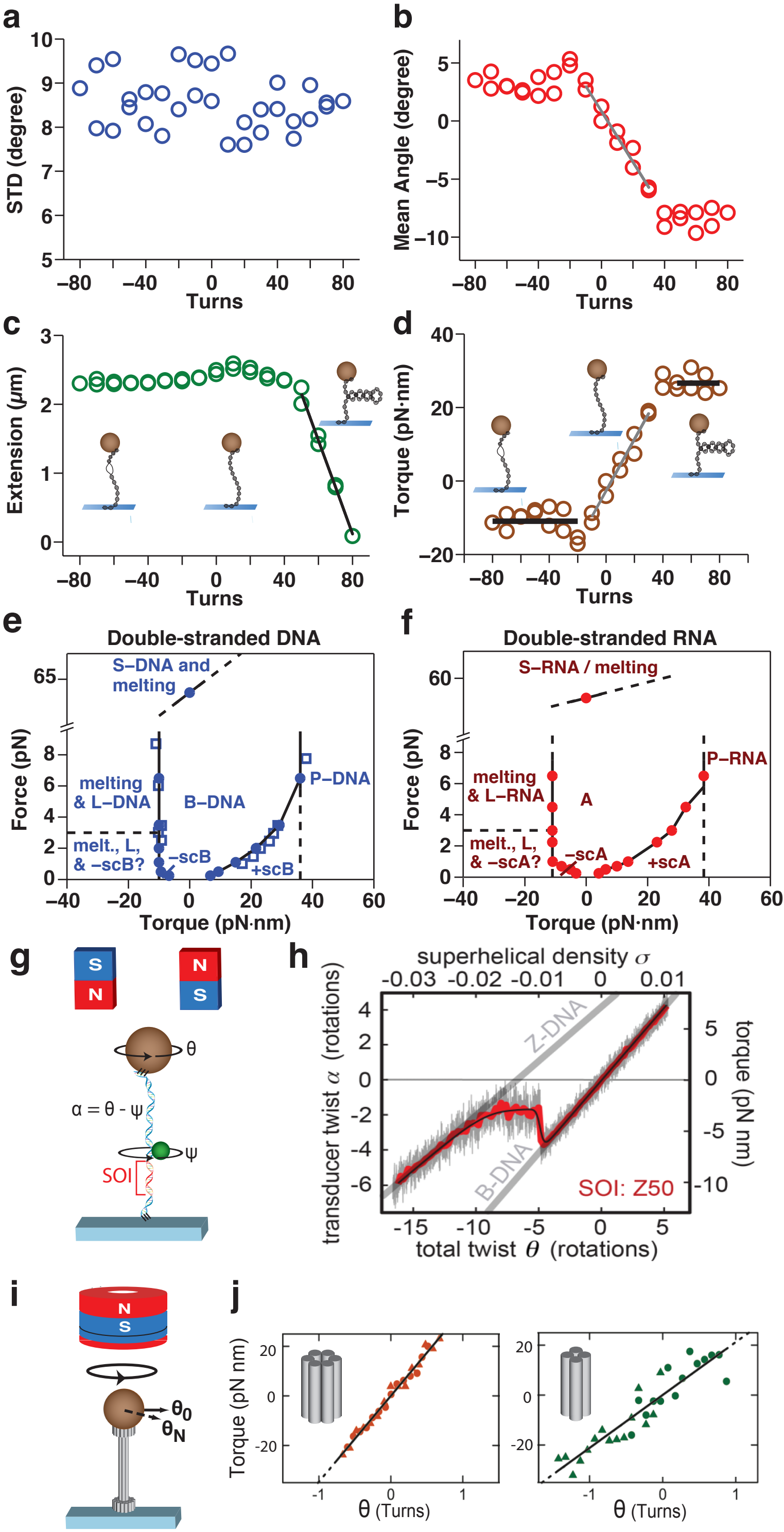
a
STD (degree)
Turns
b
Mean Angle (degree)
Turns
c
Extension (μm)
Turns
d
Torque (pN·nm)
Turns
e
Double-stranded DNA
S–DNA and melting
melting & L–DNA
B–DNA
P–DNA
melt., L, & –scB?
–scB
+scB
Force (pN)
Torque (pN·nm)
f
Double-stranded RNA
S–RNA / melting
melting & L–RNA
A
P–RNA
melt., L, & –scA?
–scA
+scA
Force (pN)
Torque (pN·nm)
g
S
N
N
S
θ
α = θ - ψ
ψ
SOI
h
superhelical density σ
Z-DNA
B-DNA
SOI: Z50
transducer twist α (rotations)
total twist θ (rotations)
torque (pN nm)
i
N
S
θ0
θN
j
Torque (pN nm)
θ (Turns)
θ (Turns)

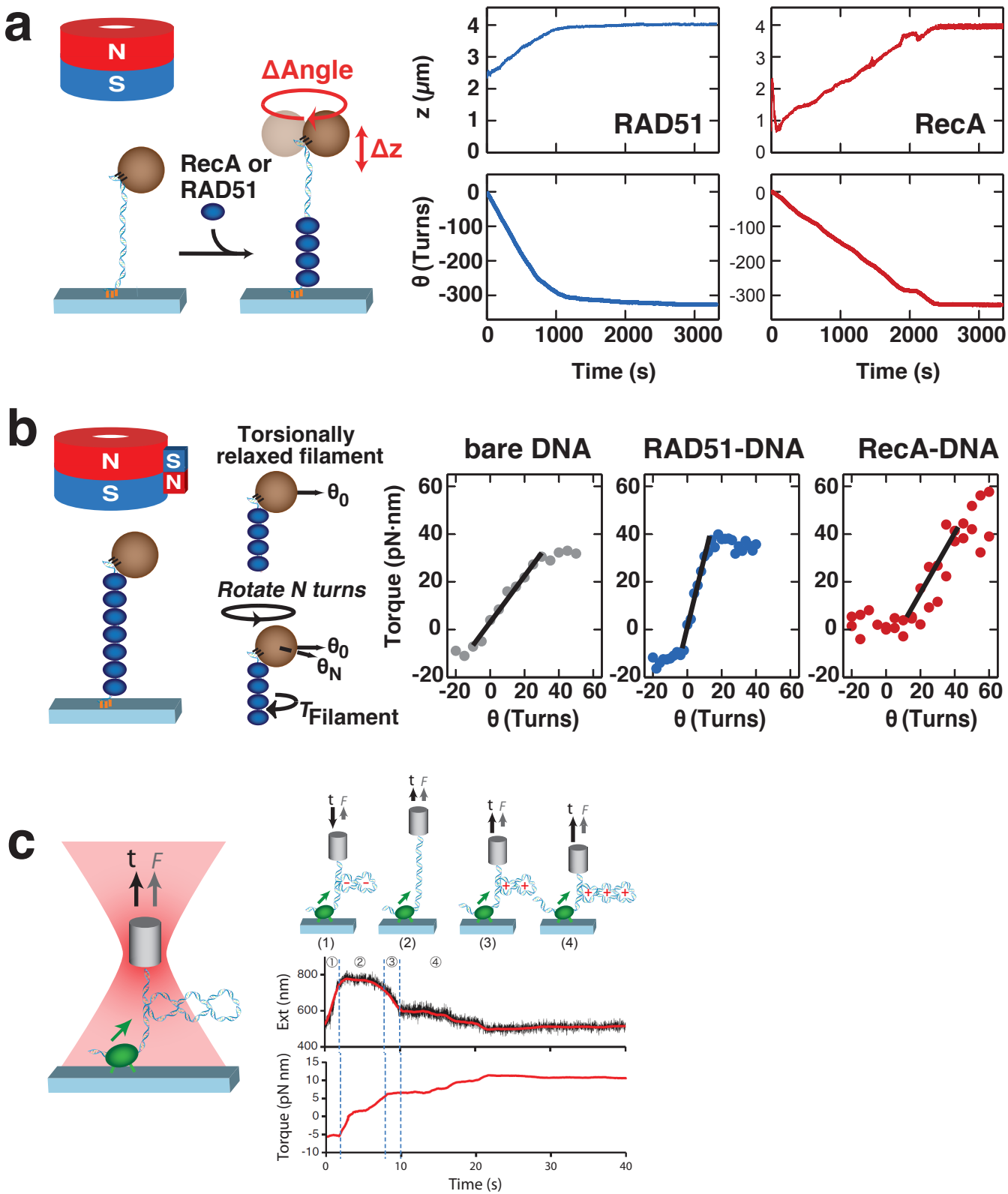
a
N
S
ΔAngle
Δz
RecA or
RAD51
z (μm)
RAD51
RecA
θ (Turns)
Time (s)
b
Torsionally
relaxed filament
θ0
Rotate N turns
θN
TFilament
bare DNA
RAD51-DNA
RecA-DNA
Torque (pN·nm)
θ (Turns)
c
t F
(1)
(2)
(3)
(4)
Ext (nm)
Torque (pN nm)
Time (s)

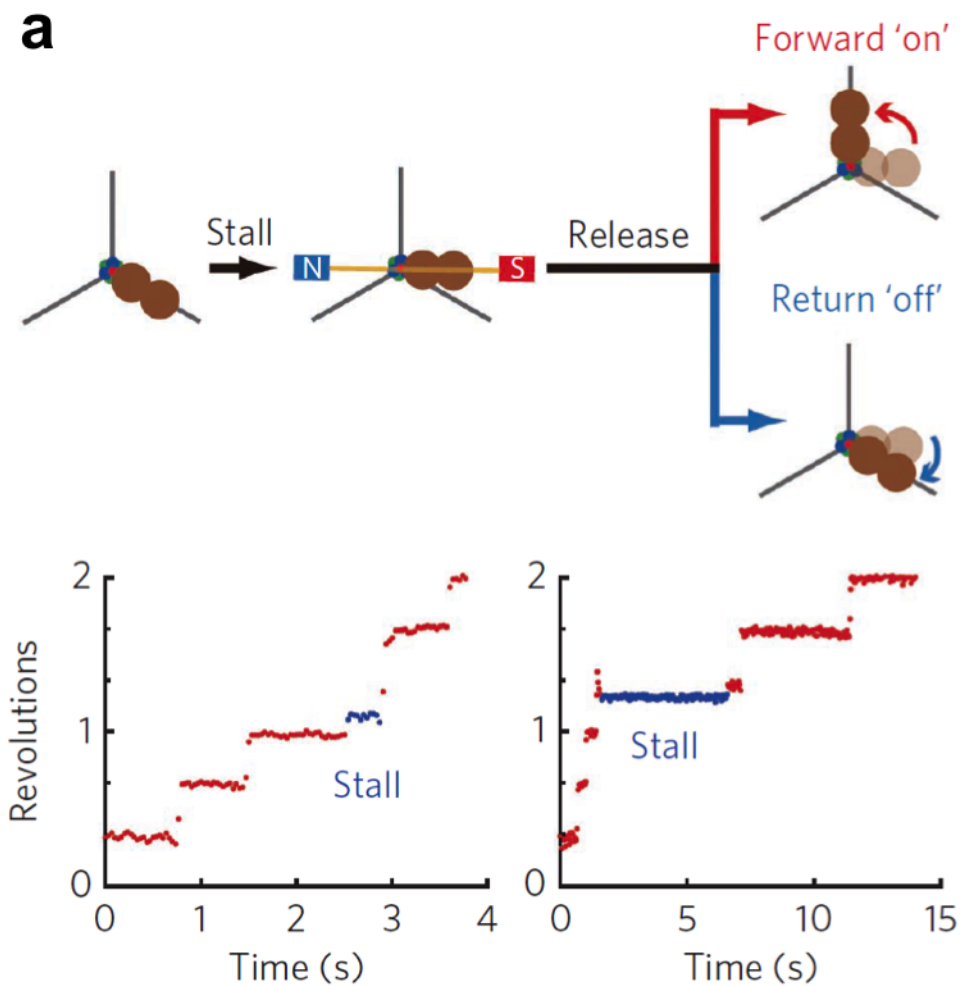

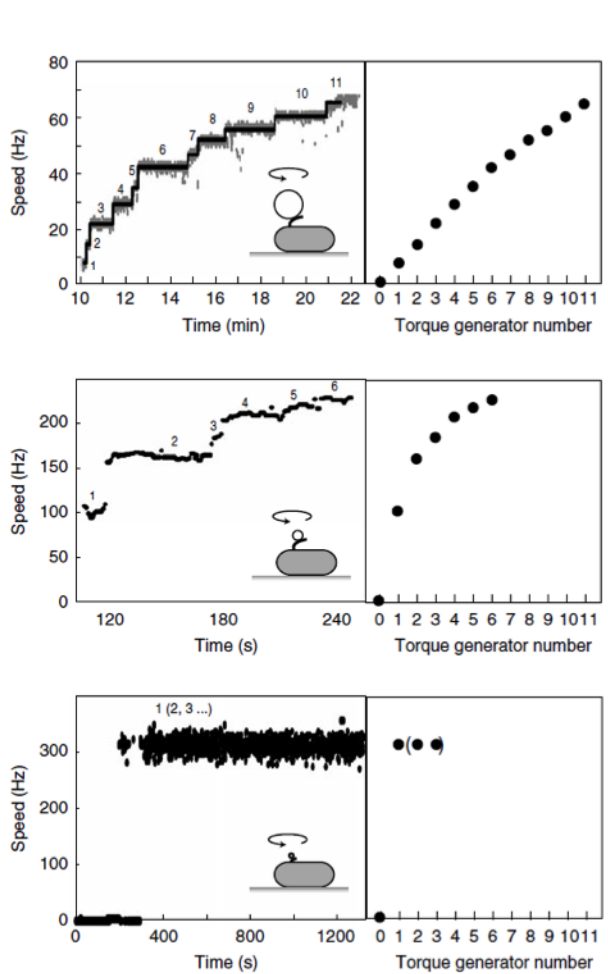

Lipfert et al., Figure 9